ARTICLE IN PRESS

Nature Communications

https://doi.org/10.1038/s41467-026-71530-9

Article in Press

Vitamin D binding protein induces skeletal muscle atrophy and contributes to cancer-associated muscle wasting independently of vitamin D status in preclinical models

Received: 18 April 2024

Accepted: 19 March 2026

Tommaso Raiteri, Simone Reano, Andrea Scircoli, Ivan Zaggia, Alessandro Antonioli, Stefania Faletti, Francesco Favero, Marcello Manfredi, Giuliana Pelicci, Davide Corà, Lorenza Scotti, Richard R. Kew, Flavia Prodam, Paolo E. Porporato & Nicoletta Filigheddu

Cite this article as: Raiteri, T., Reano, S., Scircoli, A. *et al.* Vitamin D binding protein induces skeletal muscle atrophy and contributes to cancer-associated muscle wasting independently of vitamin D status in preclinical models. *Nat Commun* (2026). https://doi.org/10.1038/s41467-026-71530-9

We are providing an unedited version of this manuscript to give early access to its findings. Before final publication, the manuscript will undergo further editing. Please note there may be errors present which affect the content, and all legal disclaimers apply.

If this paper is publishing under a Transparent Peer Review model then Peer Review reports will publish with the final article.

ARTICLE IN PRESS

© The Author(s) 2026. **Open Access** This article is licensed under a Creative Commons Attribution-NonCommercial-NoDerivatives 4.0 International License, which permits any non-commercial use, sharing, distribution and reproduction in any medium or format, as long as you give appropriate credit to the original author(s) and the source, provide a link to the Creative Commons licence, and indicate if you modified the licensed material. You do not have permission under this licence to share adapted material derived from this article or parts of it. The images or other third party material in this article are included in the article's Creative Commons licence, unless indicated otherwise in a credit line to the material. If material is not included in the article's Creative Commons licence and your intended use is not permitted by statutory regulation or exceeds the permitted use, you will need to obtain permission directly from the copyright holder. To view a copy of this licence, visit http://creativecommons.org/licenses/by-nc-nd/4.0/.

Vitamin D binding protein induces skeletal muscle atrophy and contributes to cancer-associated muscle wasting independently of vitamin D status in preclinical models

Tommaso Raiteri[1,2], Simone Reano[1,3], Andrea Scircoli[1], Ivan Zaggia[1], Alessandro Antonioli[4,2], Stefania Faletti[5], Francesco Favero[1,3], Marcello Manfredi[1,3,6], Giuliana Pelicci[1,5], Davide Corà[1,3], Lorenza Scotti[1], Richard R Kew[7], Flavia Prodam[4], Paolo E Porporato[8], Nicoletta Filigheddu[1,2*]

1 Department of Translational Medicine, University of Piemonte Orientale, Novara, Italy.

2 Interuniversity Institute of Myology (IIM), Perugia, Italy.

3 Center for Translational Research on Autoimmune and Allergic Disease (CAAD), University of Piemonte Orientale, Novara, Italy.

4 Department of Health Sciences, University of Piemonte Orientale, Novara, Italy.

5 Department of Experimental Oncology, European Institute of Oncology (IEO), IRCCS, Milan, Italy.

6 Institute for Molecular and Translational Cardiology (IMTC), IRCCS Policlinico San Donato, S. Donato Milanese (MI), Italy.

7 Department of Pathology. Stony Brook University and Stony Brook Cancer Center, Stony Brook, New York, USA.

8 Department of Molecular Biotechnology and Health Sciences, University of Torino, Turin, Italy.

Andrea Scircoli and Ivan Zaggia current affiliation: Department of Molecular Biotechnology and Health Sciences, University of Torino, Turin, Italy.

Stefania Faletti current affiliation: Fondazione Human Technopole, Milan, Italy.

*Corresponding author: Nicoletta Filigheddu, University of Piemonte Orientale, Department of Translational Medicine, Via Solaroli 17, 28100 Novara, Italy.

nicoletta.filigheddu@med.uniupo.it

Abstract

The maintenance of skeletal muscle is of pivotal importance, as its loss is often associated with progressive pathologies, generally worsening the prognosis. Increased levels of vitamin D binding protein (VDBP) were reported in diseases susceptible to muscle wasting, including several tumors. We hypothesized that VDBP might participate in muscle wasting and investigated its direct effects on skeletal muscle homeostasis. Here, we demonstrate that VDBP induces atrophy independently of vitamin D. In C2C12 myotubes, we identified intracellular actin dynamics perturbation and subsequent mitochondrial fragmentation as the main molecular mechanisms of VDBP-induced atrophy. Coherently, the ectopic introduction of VDBP in mice lacking the protein (*Gc*-knockout mice) induced muscle atrophy and decreased strength. Finally, we present proof-of-concept evidence that VDBP contributes to cancer-associated muscle wasting in Lewis lung carcinoma (LLC)-bearing male mice. Altogether, these findings provide novel insights into the biological function of VDBP as a pro-atrophic hormone with potential implications for the treatment of muscle wasting.

Introduction

Vitamin D binding protein (VDBP), also known as Group-specific component or Gc-globulin, is a multifunctional serum glycoprotein belonging to the albumin gene family. The protein is coded by the *Gc* gene and synthesized by hepatocytes, and its best-known function, as its name suggests, is the binding and transport in the bloodstream of vitamin D metabolites. Besides this task, VDBP participates in the actin-scavenger system by acting as a monomeric G-actin-sequestering agent in extracellular spaces in case of tissue damage[1]. Coherently, several works reported a decrease in circulating VDBP following acute injury, likely due to its consumption within the G-actin scavenging process, both in human conditions and animal models[2,3], followed by enhanced synthesis[4].

Furthermore, the G-actin-VDBP complex has an indirect but essential role as a cofactor for neutrophil migration, thus contributing to the inflammatory response[5]. Accordingly, mice lacking VDBP (*Gc* knockout mice; *Gc* KO) display lower inflammation in different models of inflammatory injuries, including acute muscle injury[3,6].

Interestingly, proteomic analyses revealed the upregulation of VDBP in biological fluids from patients or animal models affected by pathologies susceptible to progressive muscle wasting or cachexia, including several types of cancer[7–12], chronic kidney disease[13,14], diabetes mellitus[15], multiple sclerosis[16], Parkinson's disease[17], and COPD[18], suggesting a potential role for VDBP in skeletal muscle homeostasis. We specifically hypothesized that VDBP could induce muscle atrophy and participate in disease-associated muscle wasting. To this end, we investigated the direct effects of VDBP on skeletal muscle using the in vitro model of C2C12-derived myotubes. We showed that VDBP directly acted on muscle cells, disrupting intracellular actin dynamics and leading to mitochondrial fragmentation and atrophy, effects and mechanisms that we observed in human cells as well. We then assessed the in vivo effect of treatment with VDBP in the muscle of *Gc* KO mice through muscular injection of the protein and, finally, the involvement of VDBP in the onset and severity of cancer-associated muscle wasting, comparing Lewis lung carcinoma (LLC)-induced cachexia in *Gc* KO vs. WT mice. We showed that, similarly to human cancers, VDBP increased in this murine model of cancer cachexia, and we found that the lack of VDBP conferred protection against muscle loss. Our findings demonstrate that VDBP is an active hormone per se, with pro-atrophic effects in skeletal muscle, and one of the players of muscle wasting in cancer cachexia.

Results

VDBP induces atrophy in C2C12 myotubes and enhances mitophagy

To test the hypothesis that VDBP could induce muscle atrophy, we assessed its effect on the in vitro model of murine C2C12-derived myotubes, in which atrophy can be easily evaluated by measuring the variations in myotube diameters. We observed that VDBP induced the reduction of myotube diameter in a dose-dependent manner (Fig. 1A). The 50 nM dose was used for all the following in vitro experiments. Atrophy was induced with this dose of VDBP also on myofibers isolated from extensor digitorum longus (EDL) muscle (Fig. 1B).

The activation of the ubiquitin-proteasome system (UPS) is one of the main mechanisms involved in muscle wasting[19]. However, the atrogenes Atrogin-1 (*Fbxo32*/*MAFbx*) and MuRF1 (*Trim63*), which encode muscle-specific ubiquitin ligases and are representative of UPS activation, were not induced by VDBP treatment (Fig. 1C), suggesting that VDBP activity on skeletal muscle does not involve the UPS. Coherently, the proteasome inhibitor MG-132, able to block myotube atrophy dependent on UPS activation, such as that caused by dexamethasone treatment, had no effect on VDBP-induced atrophy (Fig. 1D).

In vitro, changes in myotube diameter can also be due to the modulation of differentiation and fusion of residual myoblasts in culture[20]. VDBP induced a slight, non-significant delay in C2C12 differentiation, seen as the reduced number of cells expressing myosin heavy chain (MyHC+), detectable only at 48 h of treatment (3.35% vs. 4.31%, non-significant). On the other hand, after 72 h of treatment, C2C12 fusion, quantified as the average number of nuclei in MyHC+ cells, was reduced by VDBP (Fig. 1E); however, the contribution of VDBP-induced impairment of residual myoblasts fusion would not account for the 15% loss in diameters observed after 24 h of treatment, since untreated myotube diameters were stable in this lapse of time (65.42 ± 6.1 µm vs. 62.03 ± 4.92 µm, non-significant).

Dysregulation of basal autophagy is another important mechanism mediating muscle catabolism, and VDBP hyperactivated autophagy in C2C12 myotubes. VDBP induced the accumulation of LC3II following the block of the autophagic flux with chloroquine (CLQ), a compound that prevents the fusion of autophagosomes with lysosomes (Fig. 1F), indicating that the decrease of LC3II upon VDBP treatment in the absence of CLQ is due to the rapid LC3II turnover. The intensified autophagic flux was not accompanied by alterations in the expression of the autophagic genes *Ctsl* (cathepsin L), *Gabarap*, and *Atg12*, while *Bnip3*, specifically involved in mitophagy[21], was slightly, although not significantly, induced (Fig. 1G), suggesting that the increased autophagy elicited by VDBP could target mitochondria. This notion was supported by the augmented co-localization, upon VDBP treatment, of MitoTracker with LysoTracker, specific probes for mitochondria and lysosomes, respectively, (Fig. 1H) and the enrichment of LC3B II in mitochondrial fractions (Fig. 1I). The enhancement of VDBP-triggered mitophagy hinted at the presence of damaged mitochondria that need to be removed.

VDBP impacts on C2C12 myotube proteome, altering actin- and mitochondrial metabolism- related proteins

To elucidate the molecular mechanisms underlying VDBP-induced atrophy, we conducted a proteomic analysis of VDBP-treated C2C12 myotubes utilizing a label-free proteomics approach. Treatments of 18 or 24 h with VDBP significantly altered the myotube proteome, as evidenced by the identification in VDBP-treated cells of 387 proteins (3 over- and 32 under-expressed, fold change ≥1.3 and p-value ≤0.05) and 1215 proteins (21 over- and 36 under-expressed, fold change ≥1.3 and p-value ≤0.05), respectively (Fig. 2A and C and Supplementary Data 1 and 2). The proteomic analyses of VDBP-treated myotubes revealed the downregulation of several proteins involved in cellular and mitochondrial metabolism and intracellular actin dynamics (Fig. 2B and D). Notably, Ingenuity Pathway Analysis (IPA) of the differentially expressed proteins after 24 h of treatment highlighted the deregulation of several proteins of the mitochondrial electron transport system (ETS), in particular, of the respiratory complex I (Supplementary Fig. 1), suggesting that VDBP could cause mitochondrial dysfunction in C2C12 myotubes.

VDBP induces mitochondrial dysfunction in C2C12 myotubes

In accord with the detected alterations of proteins related to mitochondrial metabolism upon VDBP treatment, we observed that VDBP decreased O_2 consumption in VDBP-treated myotubes (Fig. 3A-D). In particular, VDBP reduced basal respiration (i.e., routine state) and maximal respiration capacity (i.e., ET state; Fig. 3B), O_2 flux linked to ATP production (i.e., oxidative phosphorylation; Fig. 3C), and reserve respiratory capacity, a critical component of mitochondrial oxidation that can be utilized during states of increased ATP demand (Fig. 3D). The relative expression of the mitochondrial DNA (mtDNA) gene *Cox2* normalized on the genomic DNA (nDNA) gene *Rps18*, showed no significant differences between VDBP-treated myotubes and controls (Fig. 3E), suggesting that the decreased mitochondrial respiration was due to functional impairment of mitochondria rather than to their reduced content. On the other hand, the expression of peroxisome proliferator-activated receptor-gamma coactivator-1a (*Ppargc1a*), the master regulator of mitochondrial biogenesis, was induced by VDBP treatment (Fig. 3F), suggesting, together with the increased mitophagy (Fig. 1H and I), a high turnover of mitochondria promoted by VDBP. Still, VDBP altered the expression of players of mitochondrial dynamics, which, through fusion and fission events, serve to dilute damaged components of mitochondria or eliminate them through mitophagy, respectively. VDBP decreased the expression of the fusion marker *Opa1* and increased the fission marker *Mff* (Fig. 3G). Accordingly, VDBP caused a remarkable fragmentation of mitochondria (Fig. 3H), quantified as a decrease in the average area of mitochondria. Also, VDBP induced loss of mitochondrial membrane potential, highlighted by the diffusion of the cationic dye JC-1 from the mitochondria to the cytoplasm with the concomitant fluorescence emission shift from red to green (Fig. 3I), in accordance with the fact that mitochondrial fission results in mitochondrial membrane potential dissipation[22] that leads to the recruitment of the machinery needed to initiate the autophagic degradation of damaged mitochondria[23].

The altered mitochondrial respiration upon VDBP treatment increased the production of reactive oxygen species (ROS) that was abolished by co-treatment with the specific mitochondria-targeted antioxidant mitoTEMPO (Fig. 3J). Importantly, treatment of cells with mitoTEMPO completely prevented VDBP-induced atrophy (Fig. 3K), pointing at mitochondrial dysfunction as a primary cause of VDBP-induced C2C12 atrophy. Notably, mitoTEMPO treatment did not prevent VDBP-induced mitochondrial membrane depolarization (Fig. 3L), suggesting that the latter is an upstream event to ROS production.

VDBP enters C2C12 through megalin and induces atrophy by perturbing the intracellular actin dynamics, independently of vitamin D

To provide evidence that VDBP acts directly on C2C12 and rule out the possibility that atrophy could derive from the sequestering of trophic factors in the culture media, we silenced *Lrp2*, the gene coding for megalin, the endocytic receptor through which VDBP enters muscle cells[24]. *Lrp2* silencing, confirmed by real-time PCR and immunofluorescence assays (Suppl. Fig. 2), prevented VDBP-induced intracellular increase of VDBP itself (Fig. 4A), intracellular ROS rise (Fig. 4B), and C2C12 atrophy (Fig. 4C).

Although the experiments were carried out in serum-free media, therefore in the absence of extracellular vitamin D, VDBP could still alter the intracellular content of vitamin D, especially sequestering the free form of 25-hydroxy-vitamin D_3 (25VD), a protective, anti-atrophic vitamin D metabolite[25]. To exclude the possibility that the atrophic activity of VDBP is secondary to intracellular sequestration of anti-atrophic 25VD, we treated cells with VDBP pre-bound to 25VD at a 1:1 stoichiometric ratio. We observed that 25VD-bound VDBP had the same effects as VDBP alone in terms of ROS production (Fig. 4D) and myotube diameter reduction (Fig. 4E), further indicating that VDBP atrophic activity is independent of changes in intracellular 25VD availability. Of note, using specific ELISAs, we could easily detect an intracellular increase in free 25VD after treatment with 100 nM 25VD, but no differences when myotubes were treated with VDBP alone or 25VD-bound VDBP (Fig. 4F). Meanwhile, the total intracellular 25VD increased after treatment with either 25VD or 25VD-bound VDBP, as expected. Altogether, these observations further support the idea that, under serum-free conditions, there is not a relevant intracellular reservoir of anti-atrophic free 25VD that could be influenced by VDBP treatment.

In accordance with its physiological role in the G-actin scavenging system, we hypothesized that VDBP, by sequestering the intracellular G-actin in C2C12 myotubes, could perturb the cycling of intracellular actin between the G and F states, which is fundamental for many cellular processes involved in muscle homeostasis, including the control of mitochondrial dynamics[26]. Coherently with previous data on C2 myotubes[24], VDBP was able to bind intracellular actin, as seen by immunoprecipitation assay (Fig. 4G), thus altering the intracellular G-/F-actin ratio (Fig. 4H). To assess if the derangement of the physiological G-/F-actin balance could represent the mechanism responsible of VDBP-induced atrophy in C2C12, we pre-treated the cells with jasplakinolide (Jas), a stabilizer of the intracellular polymerized F-actin. Remarkably, Jas-mediated F-actin stabilization totally prevented VDBP-induced ROS production, mitochondrial membrane depolarization, and myotube diameter reduction (Fig. 4I-K).

VDBP-induced perturbation of intracellular actin dynamics promotes mitochondrial fission and myotube atrophy in murine and human cells

Coherently with VDBP shuttling role between the plasma membrane and mitochondria[27], VDBP and VDBP-actin complexes accumulated in these organelles (Fig. 5A and B). We hypothesized that the increased mitochondria-located actin and its cycling between G- and F-forms could recruit dynamin-related protein 1 (DRP1), a fundamental requirement for fission to occur[22]. Indeed, we observed the mitochondrial accumulation, in VDBP-treated myotubes, of DRP1 (Fig. 5C) and, in addition, a proximity ligation assay (PLA) performed between DRP1 and VDBP showed that VDBP induced an increase of puncta that was prevented by Jas treatment (Fig. 5D). To assess the role of DRP1 in VDBP-induced atrophy, we treated C2C12 myotubes with 10 μM Mitochondrial division inhibitor 1 (Mdivi-1), a non-toxic, non-atrophic dose of the specific pharmacological inhibitor of DRP1[28,29]. The complete prevention of VDBP-induced ROS production and myotube diameter reduction (Fig. 5E and F) indicates a central role of DRP1 in VDBP-induced atrophy.

Notably, VDBP effects were reproducible in myotubes derived from the differentiation of human myoblasts as well. Treatment of human myotubes with VDBP induced mitochondrial fragmentation, an increase in ROS production, and a decrease in myotube size (Fig. 5G-I), and both Jas and Mdivi-1 fully reverted these effects, indicating that, also in human myotubes, VDBP acts through dysregulation of intracellular actin dynamics and DRP1 recruitment at the mitochondria.

VDBP induces skeletal muscle atrophy in vivo

To determine if VDBP has a causative role in muscle wasting in vivo as well, we exploited *Gc* KO male mice[6], in which we injected 1.5 mg/kg VDBP every 48 h for an overall 8-day experimental period in tibialis anterior (TA) muscles using the corresponding saline-injected contralateral muscle as controls.

VDBP-treated mice showed a significant loss of grip strength compared to the controls starting from 48 h (Fig. 6A), and a small subset of mice (n=4) were analyzed at this time point. However, the decrease in force was not accompanied by a reduction in TA muscle weight (Fig. 6B). Nevertheless, VDBP-injected TA muscles displayed a fiber shift, with a significant reduction in type IIa fibers and the tendency of an increase in type IIb fibers (Fig. 6C). Similarly to the in vitro results, VDBP induced the alteration of G-/F-actin balance (Fig. 6D) and an increase in *Mff* expression (Fig. 6E), while *Bnip3* and *Ppargc1a* expression were not significantly altered (Fig. 6F and G). The unaltered overall levels of the mitochondrial protein TOM20 suggest stable mitochondrial content (Fig. 6H). However, mitochondria appeared to be fragmented in the VDBP-treated muscles (Fig. 6I), and mitochondrial respiration was slightly impaired (Fig. 6J). After 8 days of treatment, there was an appreciable decrease in TA muscle weight (Fig. 6K) accompanied by a shift towards smaller areas in the fiber cross-sectional area (CSA) frequency distribution of VDBP-injected muscles (Fig. 6L). The fiber type shift consolidated, with a significant increase of fiber type IIx and IIb, in addition to the decrease in type IIa (Fig. 6M). Of note, no changes were observed in the adjacent gastrocnemius and quadriceps muscles (Suppl. Fig. 3), indicating that VDBP did not diffuse beyond the injection site.

The induction of *Mff* was enhanced (Fig. 6N). Both the mitophagy marker *Bnip3* and the mitochondrial biogenesis marker *Ppargc1a* were strongly induced (Fig. 6O and P), while the levels of TOM20 remained unchanged (Fig. 6Q), collectively suggesting the activation of mitochondrial quality control and turnover. Coherently, mitochondria of VDBP-injected muscles appeared more fragmented (Fig. 6R), and their respiratory function was impaired (Fig. 6S). Similarly to what was observed in vitro (Fig. 4F), VDBP injection did not alter the local levels of free 25VD (Fig. 6T), thus ruling out the possibility that VDBP atrophic effect is caused by the depletion of anti-atrophic free 25VD.

VDBP participates in cancer-associated muscle wasting

Coherently with the upregulation of VDBP observed in cancer patients, also the Lewis lung carcinoma (LLC) murine model of cancer cachexia was characterized by increased VDBP, seen in male mice, both as *Gc* transcript in the liver, the main organ producing VDBP, (Fig. 7A) and VDBP protein in blood (Fig 7B). Notably, the contribution of the tumor to the VDBP increase appears negligible, as *Gc* transcript levels in the tumor are almost undetectable compared to those in the liver (Fig. 7A).

To determine whether VDBP plays a role in the development of cancer-induced cachexia, we subcutaneously implanted LLC cancer cells into *Gc* KO and wild-type (WT) male mice and monitored the effects of the lack of VDBP in the development of cachexia for 3 weeks. Notably, this cachexia model is characterized by unaltered vitamin D levels[30]. We corroborated this evidence by demonstrating that both the total and the free 25VD did not change in the blood of tumor-bearing mice (Fig. 7C). The same was true for *Gc* KO mice, although, as expected[31], they have constitutively lower levels of the hormone. Remarkably, the free 25VD, the form that could be bound by VDBP, was unaltered in WT and *Gc* KO muscles, independently of the presence of tumor.

To further assess if the two genotypes had comparable whole-body metabolism, we performed glucose and insulin tolerance tests and measured energy expenditure using indirect calorimetry in *Gc* KO and WT mice. We confirmed previously published data showing no significant differences in glucose and insulin tolerance tests[32] and found no differences in energy expenditure between the two genotypes (Suppl. Fig. 4A-C), ruling out the likelihood that baseline metabolic differences could influence cachexia development. In addition, energy expenditure increased equally during cachexia in both genotypes (Suppl. Fig. 4D).

During cachexia progression, WT mice exhibited a significant decline in muscle strength compared to *Gc* KO mice, beginning on day 7 after LLC injection and persisting until the end of the experimental period (Fig. 7D). Consistently, exercise capacity at the endpoint, assessed through a treadmill exhaustion test, was lower in WT than in *Gc* KO mice (Fig. 7E). WT mice lost approximately 10% of total body weight, whereas *Gc* KO mice maintained their initial weight (Fig. 7F). Importantly, between the two groups, there were no significant differences in food intake nor tumor growth (Suppl. Fig. 4E and F). Coherently with body weight loss and impairment of muscle functionality, WT mice tended to lose muscle mass, while *Gc* KO mice preserved it (Fig. 7G). CSA distribution in gastrocnemius revealed larger fibers in muscles from cachectic *Gc* KO mice compared to cachectic WT mice (Fig. 7H), demonstrating that the lack of VDBP partially protects mice from tumor-induced muscle wasting. Notably, no fiber type switch was detected in either genotype under cachectic conditions (Suppl. Fig. 4G).

Despite in vitro VDBP-induced atrophy being independent of atrogene induction (Fig. 1C), Atrogin-1 was transcriptionally upregulated in the muscles from cachectic WT mice, while the induction in *Gc* KO mice was not significant (Fig. 7I). On the other hand, *Bnip3* and

Mff expression increased, either significantly or as a trend, only in WT tumor-bearing mice (Fig. 7J and K). Accordingly, we observed mitochondrial fragmentation in the muscles of tumor-bearing mice, which was milder in *Gc* KO mice (Fig. 7L), coherently with the in vitro data and the results of VDBP intramuscular injection in muscles, where VDBP induced mitochondrial fragmentation.

Consistently, mitochondrial respiration appeared to be impaired only in WT cachectic mice (Fig. 7M).

Notably, in WT mice, LLC-induced cachexia affected neuromuscular junction (NMJ) morphology and innervation, while, in *Gc* KO tumor-bearing mice, NMJ were preserved (Fig. 7N).

RNA-seq analysis revealed the involvement of inflammatory pathways and atrogenes in cachectic WT mice only

To further understand the impact of VDBP in cancer-associated muscle wasting and the molecular pathways involved, we performed an RNA-seq analysis on the gastrocnemii from tumor-bearing mice compared to the corresponding controls in WT and *Gc* KO mice.

The RNA-seq analysis revealed the common and different differentially expressed genes (DEGs) characterizing the two genotypes. The presence of LLC induced the deregulation of 267 genes in WT mice and 109 in *Gc* KO mice (Fig. 8A and Supplementary Data 3). As shown by Venn diagrams, intersection between the sets of modulated genes identified a total of 186 DEGs belonging to WT mice only, 28 as belonging to the *Gc* KO mice only, and 81 DEGs in common to both groups (Fig. 8B). Coherently with the atrophic phenotype, only cachectic WT mice showed the increased expression of atrogenes, such as *Fbxo32*, *Trim63*, *Gadd45*, *Retreg1*, *Depp1*, and *Cdkn1a*. The increased expression of *Fbxo32* in tumor-bearing WT mice

(Supplementary Data 3) is congruous with the real-time PCR data of Fig. 6I, showing a significant induction of this atrogene in cachectic muscles from WT mice only. Nevertheless, the majority of DEGs in WT cachectic muscles were related to enhanced inflammation and immune response, such as the transcription factor *Cebpb*, the complement factor *C4b*, the cytokines *Ccl6* and *Ccl9*, and *Mmp9*. In tumor-bearing *Gc* KO mice, on the contrary, the RNA-seq analysis revealed a strong down-regulation of different collagen genes (*Col5a3*, *Col8a2*, *Col11a2*, *Col16a1*), two serpins (*Serpina1c* and *Serpina1d*), and *Arg1* (Supplementary Data 3). Comparing the WT and *Gc* KO tumor-bearing mice, gene set enrichment analysis (GSEA) revealed the upregulation, in cachectic WT muscles, of the gene sets "TNFa signaling via NF-kB", "hypoxia", and "apoptosis", while, in *Gc* KO tumor-bearing mice the enriched categories were "epithelial-mesenchymal transition", "apical junction", and "angiogenesis" (Fig. 8C). Interestingly, IPA analysis of upstream regulators (Supplementary Data 4) predicted the activation of several genes that control the expression of inflammation-related genes and atrogenes, including *Tnf*, *Il6*, *Stat3*, and *Foxo3* in WT cachectic samples. Conversely, among the few upstream regulators predicted to be inhibited, the analysis identified *Sirt1*, which physiologically inhibits atrogene induction[33]. On the other hand, for cachectic *Gc* KO mice, the limited number of DEGs allowed identifying only one upstream regulator, namely *Pparg*, predicted to be downregulated.

Discussion

Our results demonstrate that VDBP can exert hormone-like, pro-atrophic effects on skeletal muscle and may contribute to muscle wasting in conditions where VDBP is elevated, including cancer cachexia.

VDBP binds and carries vitamin D both to different tissues within the body and from the cell surface to mitochondria, where it undergoes the multiple hydroxylation steps occurring during its metabolism[27]. However, VDBP has many other physiological roles[34], including its participation in the actin-scavenger system, thanks to its ability to bind monomeric G-actin. This mechanism, which is activated in case of severe tissue damage, restrains the intracellular G-actin released into extracellular spaces from polymerizing into F-actin, thus preventing the formation of occlusions[1]. Our data suggest that the atrophic effect of VDBP on muscle cells depends on its ability to bind intracellular G-actin, thus perturbing the physiological cycling between G- and F-actin. This dysregulation might affect several cellular functions, including motility, contraction, and division, as well as gene expression. For instance, intracellular G-actin polymerization liberates G-actin-binding proteins, such as myocardin-related transcription factors (MRTFs), allowing their nuclear translocation and the modulation of the activity of their transcriptional cofactors, one of which is serum response factor (SRF). In the context of skeletal muscle, G-actin polymerization and the actin-MRTF-SRF pathway contribute to muscle mass maintenance[35–37], and it is downregulated in sarcopenia[38] and in denervation-induced muscle atrophy[39]. We speculate that VDBP sequestering of G-actin induced a compensatory depolymerization of F-actin in an effort to maintain the equilibrium between the two forms, thus locally perturbing the amount of F-actin. In the long run, this could have an inhibitory effect on the actin-MRTF-SRF axis, favoring the onset of muscle atrophy. Accordingly, the RNA-seq analysis of cachectic muscles of tumor-bearing mice with increased levels of VDBP showed a reduction of *Mrtfa* (Supplementary Data 3).

However, our data align with a more direct mechanism where the atrophy-inducing effect is mediated by the accumulation of VDBP-actin complexes on mitochondria that putatively induce a local perturbation of actin dynamics, thus facilitating the recruitment of DRP1 and subsequent mitochondrial fission.

Remarkably, another G-actin binding protein, i.e., cofilin1, has been shown to be essential for inducing mitochondrial fission and mitophagy in breast cells[22,40] through the enrichment of G-actin on the mitochondrial outer membrane, its local polymerization on the fission site, DRP1 recruitment, and constriction of mitochondria[41]. A similar VDBP-induced perturbation of actin dynamics in C2C12 mitochondria could explain the observed increased expression of DRP1 receptor (Mff) and the enrichment of DRP1 in mitochondria. Mitochondria fission, in turn, results in mitochondrial membrane potential dissipation[22] and mitophagy[24].

In myotubes of both murine and human origin, perturbation of actin dynamics and mitochondrial fission play a pivotal role in VDBP-induced atrophy, since F-actin stabilization through jasplakinolide or inhibition of mitochondrial fission with Mdivi-1 prevented ROS increase and atrophy.

In vivo as well, VDBP produced effects ascribable to dysregulation of actin dynamics that eventually resulted in mitochondrial fragmentation and loss of muscle mass and force.

Increased levels of VDBP have been reported in pathologies often associated with muscle wasting or cachexia, including several tumors[7–12]. Since cancer cachexia in humans is often associated with low levels of vitamin D[42], the increased VDBP could easily lead to the idea of a VDBP-mediated reduction in vitamin D bioavailability. However, our data demonstrated that the effects of VDBP on skeletal muscle cells are independent of changes in vitamin D levels. As a matter of fact, the in vitro experiments were performed in serum-free conditions, eliminating any contribution from vitamin D present in the bovine or horse sera used in the cell cultures.

Although VDBP might affect the intracellular storage of vitamin D, on which cells could rely to maintain their size, our results contradict this possibility. Indeed, VDBP did not change the amount of intracellular free 25VD (Fig. 4F). Accordingly, pre-saturation of VDBP with 25VD before treating C2C12 myotubes to prevent any possible sequestering of intracellular vitamin D did not prevent ROS induction and atrophy (Fig. 4D and E). In addition, the LLC cachexia model used in this study is characterized by unaltered vitamin D levels as previously reported[30] and confirmed by assessment of changes in levels of both free and total 25 VD in the blood of WT mice (Fig. 7C). In addition, in accordance with previous reports[31], we verified that *Gc* KO mice have reduced levels of circulating total and free 25VD and observed no further changes in the presence of the tumor. These observations rule out the possibility that *Gc* KO mice are protected from atrophy by higher 25VD levels, further supporting the notion that VDBP effects are independent of vitamin D status.

With the induction of cancer cachexia in *Gc* KO mice, we provided a proof-of-concept of the contribution of VDBP to muscle loss in pathologies with increased expression of VDBP, as mice lacking VDBP were more resistant to muscle wasting and prone to maintain muscle force.

The maintenance of muscle mass and functionality in tumor-bearing *Gc* KO mice can also be due, in part, to the preservation of NMJs. Notably, AChR clustering, an essential step of NMJ formation and stability, needs actin polymerization[43,44]. Moreover, mitochondrial integrity itself can be implicated in the maintenance of NMJs, a process requiring ATP-dependent trafficking of synaptic vesicles. For example, depletion of complex I has been shown to alter NMJ morphology, allegedly through increased ROS production[45]. ROS increase in muscles has been indeed demonstrated to induces NMJ disruption[46].

It has already been reported that cancer cachexia can alter several players crucial for the formation and stability of NMJs, including bone morphogenetic protein (BMP), muscle-specific kinase (MuSK), neural cell adhesion molecule (NCAM), and rapsyn[47–49]. However, the genes encoding such proteins were not among the DEGs of our RNA-seq, likely due to the very late stage of muscle wasting. Nevertheless, overall, the results from the RNA-seq analysis of WT cachectic muscles were highly concordant with previously published data on LLC-induced muscle wasting[50]. The fact that most of the DEGs involved in skeletal muscle atrophy were found in the WT genotype only is consistent with the protection from cancer-associated muscle wasting observed in *Gc* KO mice. Both cancer-bearing genotypes showed the upregulation of some genes involved in inflammation or inflammatory response, such as *Il1b*, *Ccl8*, *Ccr1*, and *Clec4d/4e* (Supplementary Data 3), but only WT mice seemed to be affected, at least at the muscular level. The substantial loss of muscle mass in WT compared to *Gc* KO mice can be a consequence of the pro-inflammatory activity of VDBP, which can induce selective recruitment of neutrophils[5]. Coherently, pre-cachectic and cachectic patients show increased neutrophil count compared to non-cachectic patients[51]. Neutrophils, in turn, contribute to the onset and progression of cancer cachexia by adhering to myotubes and inducing oxidative stress[52]. Likewise, the induction of atrogenes only in WT tumor-bearing mice, which seems to contradict the in vitro results, can be explained as a consequence of VDBP-induced inflammation. Both GSEA and the upstream regulators' analyses indeed proposed the pathways revolving around TNFα and IL6 to be central in VDBP-mediated atrophy in vivo.

The major effect on the muscles of tumor-bearing *Gc* KO mice was the downregulation of several collagens. Although collagen is the most abundant component of the extracellular matrix in skeletal muscle and is important for the mechanical support of the tissue, the upregulation of collagen in skeletal muscle of cachectic patients has been linked with poor survival[53]. Notably, in these patients, it was also reported the upregulation of serpine1, a downstream target of TGF-β that mediates tissue fibrosis. Coherently, in muscles of tumor-bearing *Gc* KO mice, RNA-seq analysis revealed the downregulation of *Serpine1c/d*. Therefore, the downregulation of collagen genes in the muscle of tumor-bearing *Gc* KO mice might represent a favorable trait, putatively preventing the replacement of muscle tissue with fibrotic tissue, a typical feature of cachectic muscles.

In cachectic *Gc* KO mice, IPA analysis identified *Pparg* as the only significant upstream regulator. In hepatoma-bearing rats, *Pparg* was observed to increase in cachectic skeletal muscle[54]. In *Gc* KO mice, *Pparg* was predicted to be inhibited, in accordance with the clear resistance to cancer-associated muscle wasting of these mice.

In summary, we demonstrated that VDBP-induced perturbations in intracellular actin dynamics have catastrophic effects that eventually lead to muscle wasting. Our study also provides proof-of-concept evidence showing that increased levels of VDBP associated with cancer can contribute to muscle wasting.

We believe that strategies aimed at targeting VDBP will therefore be especially important in cancer cachexia, where muscle wasting not only worsens prognosis but could also promote tumor growth and progression[55], as well as in other conditions characterized by elevated VDBP levels.

While our data support pro-atrophic actions of VDBP in skeletal muscle, several limitations should be considered. For a start, our proof-of-concept experiment on cancer cachexia was conducted solely in male mice, not addressing potential sex differences in the results.

Additionally, although systemic VDBP deletion was muscle-sparing in tumor-bearing mice, this phenotype could result from both muscle-intrinsic effects and indirect systemic mechanisms, especially those related to VDBP-associated inflammation. Also, despite the loss of the atrophic response upon megalin silencing in C2C12 myotubes supports an uptake-dependent mechanism of atrophy induction, we did not directly measure extracellular versus intracellular VDBP pools in vivo, so we cannot definitively rule out additional extracellular contributions under pathophysiological conditions.

Finally, even though key mechanistic findings were confirmed in human myotubes, our study does not provide direct evidence in humans linking VDBP variation to a skeletal muscle phenotype. Therefore, the clinical relevance of this atrophic mechanism in patients will need to be validated by future human studies.

Methods

Reagents

The following reagents were used: human VDBP (GC-Globulin, Human Plasma, Mixed Type, Athens Research and Technology; 16-16-070307); MitoTracker Green FM (Thermo Fisher Scientific; M7512), LysoTracker Red DND-99 (Thermo Fisher Scientific; L7528), JC-1 Dye (Thermo Fisher Scientific; AG-CR1-3568), and CellROX R Deep Red Reagent (Thermo Fisher Scientific; C10491); Jasplakinolide (Tocris, Bio-Techne srl; 2792); Mdivi-1 (Merck Life Sciences; 475856) Alexa Fluor 488-conjugated DNase I (Thermo Fisher Scientific; D12371); Alexa Fluor 633-conjugated Phalloidin- (Thermo Fisher Scientific; A22284). The primary and secondary antibodies and the dilutions used in this study are listed in Supplementary Table 1. All other reagents, unless otherwise stated, were from Merck Life Sciences.

Cell culture, myofiber isolation, treatments, and myotube analysis

C2C12 myoblasts (91031101, ECACC) were grown at low density in DMEM (Gibco, Thermo Fisher Scientific) supplemented with 10% fetal bovine serum (FBS, Gibco, Thermo Fisher Scientific), 100 U/mL penicillin, 100 μg/mL streptomycin, and 0.25 μg/mL antimycotic in a humidified 5% CO_2 incubator at 37 °C. To induce differentiation, cells were allowed to become confluent, and the medium was switched to differentiation medium (DM), consisting of DMEM supplemented with 2% horse serum (GE Healthcare BioSciences), penicillin, streptomycin, and antimycotic as described above. Unless otherwise specified, myotubes were treated in serum-free medium after at least 5 days of differentiation. Myotube diameters were measured with JMicroVision 1.2.7 software as previously described[56]. For every experiment assessing myotube diameters, at least 10 myotubes for each field, 5 different fields for each replicate, 3 technical replicates for each treatment were measured. Unless otherwise stated, displayed data are the means of three independent experiments.

Single myofibers were isolated as previously described[57]. Briefly, EDL muscles from C57BL/6 mice were digested in 0.2% collagenase type-I in DMEM for 60–70 min at 37 °C. Muscles were mechanically dissociated, and single fibers liberated. After extensive washing, myofibers were cultured in low proliferation medium (LPM, DMEM supplemented with 10% HS and 0.5% CEE) in suspension. Treatments were added in LPM immediately after fiber seeding, and 24 h later fibers were fixed in 4% paraformaldehyde (PFA) for 10 min. Myofiber microphotographs (10 per treatment, 10X magnification) were acquired with a bright field microscopy (Leica), and fiber diameters were measured with JMicroVision software.

Human primary cells (P01062-17M, William Cook Europe ApS), kindly provided by E. Angelino, were used between passages 11 and 15, cultured in MyoTonic™ Basal Medium (MB-2222, William Cook Europe ApS) supplemented with 10% MyoTonic™ Growth Supplement (MS-3333, William Cook Europe ApS), and differentiated by switching culture medium to MyoTonic™ Differentiation Medium (MD-5555, William Cook Europe ApS) for 5 days.

Lewis lung carcinoma (LLC) cells (CRL-1642, ATCC), kindly provided by P. Costelli (University of Torino), were cultured in DMEM containing 10% FBS, 100 U/mL penicillin, 100 μg/mL streptomycin, and 0.25 μg/mL antimycotic in a humidified 5% CO_2 incubator at 37° C.

RNA extraction and gene expression

Total RNA from myotubes or 50 mg of tissue was extracted by NucleoZOL (Macherey-Nagel). The RNA was retro-transcribed with the High-capacity cDNA Reverse Transcription Kit (Applied Biosystems, Thermo Fisher Scientific), and real-time PCR were performed with the StepOnePlus Real-time PCR System (Applied Biosystems, Thermo Fisher Scientific), using the following TaqMan probes (Thermo Fisher Scientific): *Opa1* (Mm00453873_m1), *Mff* (Mm01273401_m1), *Bnip3* (Mm01275600_g1), *Gabarap* (Mm00490678_m1), *Ctsl* (Mm00515597_m1), *Atg12*, (Mm00503201_m1), *Ppargc1a* (Mm01208835_m1), *Lrp2* (Mm01328171), *Fbxo32* (Mm00499523_m1), *Trim63* (Mm01185221_m1), *Ppif* (Mm00506384_m1), and *Gusb* (Mm01197698_m1).

Fusion index

For fusion index quantification, myotubes were fixed in 4% PFA for 10 min, permeabilized with 0.2% Triton X-100 for 5 min and blocked with 4% bovine serum albumin (BSA) for 30 min. Cells were incubated with the primary antibody to detect MyHC overnight (ON) at 4 °C and then with Alexa Fluor anti-Mouse 546 secondary for 1 at room temperature (RT), followed by 5 min of DAPI (4,6-diamidino-2-phenylindole; 1:100, Thermo Fisher Scientific). Images were acquired with an EVOS™ XL Core Imaging System (Thermo Fisher Scientific) and quantification was performed with ImageJ FIJI software v1.54p (Ashland, OR, USA).

Fusion index was calculated as average number of nuclei in myotubes with at least 3 nuclei above the total nuclei, as previously described[58].

MitoTracker and Lysotracker colocalization

Mitophagy was assessed by confocal microscopy following dual staining of mitochondria and lysosomes. C2C12 myotubes were cultured and treated in µ-Dish$^{35\text{ mm, high}}$ (Ibidi GmbH). At the end of the indicated treatments, cells were incubated with 100 nM MitoTracker Green FM and 50 nM LysoTracker Red DND-99 for 45 min at 37 °C in 5% CO_2. Following incubation, the excess of fluorophores was removed by washing with PBS, and live-cell imaging was performed using a Leica TCS SP8 confocal laser scanning microscope using a 63× immersion objective. Colocalization of mitochondria and lysosomes was quantified as Pearson's coefficient using the JACoP plugin[59] for ImageJ. This coefficient represents the overlap of the signals and can vary between -1 and 1, with R = 1 indicating a complete colocalization between the two signals.

Western blotting

At the end of the indicated treatments, cells were washed in ice-cold phosphate-buffered saline (PBS) and solubilized with a lysis buffer containing 1% Triton X-100, 0.1% sodium deoxycholate, 0.1% sodium dodecyl sulfate (SDS), 1 mM EDTA, 1 mM EGTA, 50 mM NaF, 160 mM NaCl, 20 mM Tris-HCl, pH 7.4, and supplemented with protease inhibitor cocktail. Lysates were stirred at 4 °C for 15 min and centrifuged at 15,000 × *g* for 15 min at 4 °C. Protein concentration was determined by BCA protein assay kit. Proteins were resuspended in sample buffer containing 2% SDS, 150 mM dithiothreitol (DTT), and 0.01% bromophenol blue, and 20 µg protein/lane were separated by 10 or 15% SDS-PAGE and transferred to PVDF. Membranes were saturated with 4% BSA, probed with the primary antibodies ON, washed with Tris-buffered saline (TBS) 0.1% Tween, incubated with the appropriate secondary antibody for 1 at RT, visualized with Western Lightning Chemiluminescence Reagent Plus (Perkin Elmer Life and Analytical Sciences), acquired with ChemiDoc Touch (Bio-Rad), and analyzed with ImageLab (Bio-Rad). Autophagic flux was assessed in C2C12 myotubes treated for 24 h with VDBP in the presence or absence of 10 μM chloroquine (CLQ) and calculated as the average ratio of LC3II/LC3I in CLQ-treated samples and LC3II/LC3I in CLQ-untreated cells, normalized to the signals of untreated cells.

Cellular fractionation

At the end of the indicated treatments, cells were trypsinized, resuspended in the fractionation buffer (20 mM HEPES, 10 mM KCl, 2 mM $MgCl_2$, 1 mM EDTA, 1 mM EGTA, pH 7.4), supplemented with protease inhibitor cocktail, and incubated for 15 min on ice. Cells were then lysed with a 29-gauge needle and incubated again on ice for 20 min. Afterwards, lysates were centrifuged at 720 × *g* for 5 min at 4 °C to remove the nuclei. The supernatant was centrifuged once again at 10,000 × *g* for 5 min at 4 °C. The pellet, which contains the mitochondrial fraction, was resuspended in TBS 0.1% SDS and sonicated briefly to obtain mitochondrial lysate, while the supernatant was collected and used as the cytoplasmic fraction. For each experiment, the fractionation efficacy was evaluated through western blotting, assessing the presence of cytosolic- or mitochondrial-specific markers in the corresponding fractions.

Both the mitochondrial and cytosolic fractions were then analyzed by western blotting.

Proteomics analysis

C2C12 myotubes treated with VDBP for 18 h or untreated (controls), n=3 biological replicates for each condition, were collected, washed, and lysed with RIPA buffer and denatured with

2,2,2-trifluoroethanol and then subjected to reduction with DTT 200 mM, to alkylation with iodoacetamide 200 mM and to complete protein digestion with 2 μg of trypsin. The peptide digests were desalted on the Discovery® DSC-18 solid phase extraction (SPE) 96-well plate (25 mg/well). After the desalting process, the sample was vacuum-evaporated and reconstituted in mobile phase for the analysis[60]. The digested peptides from cells collected after 18 hours of treatment were analyzed in two phases: a data-dependent acquisition (DDA) followed by data-independent analysis (DIA) on the same sample using the same gradient conditions with a micro-LC Eksigent Technologies system interfaced with a 5600+ TripleTOF system (SCIEX), as previously reported[61]. The DDA files were searched against the mouse UniProt Swiss-Prot reviewed database containing human proteins using Protein Pilot software v. 4.2 (SCIEX) and Mascot v. 2.4 (Matrix Science Inc.). Quantification was performed by integrating the extracted ion chromatogram of all the unique ions for a given peptide. Spectral alignment of the SWATH samples (DIA run) was carried out with PeakView 2.2 (SCIEX) using the spectral library generated above and the following parameters: 6 peptides per protein, 6 transitions per peptide, XIC extraction window of 5 min and a width of 15 ppm. Shared peptides were excluded as well as peptides with modifications. Peptides with FDR lower than 1.0% were exported in MarkerView 1.2 (SCIEX) for the t-test.

The digested peptides from C2C12 myotubes treated with VDBP for 24 h or untreated (controls), n=4 biological replicates for each condition, were analyzed with a UHPLC Vanquish system (Thermo Fisher Scientific) coupled with an Orbitrap Q-Exactive Plus (Thermo Fisher Scientific). Peptides were separated by a reverse phase column (Accucore™ RP-MS 100 x 2.1 mm, particle size 2.6 μm). The column was maintained at a constant temperature of 40 °C at a flow rate of 0.200 mL/min. Mobile phase A and B were water and acetonitrile, respectively, both acidified with 0.1% formic acid. The analysis was performed using the following gradient: 0-5 min from 2% to 5% B; 5-55 min from 5% to 30% B; 55-61 from 30% to 90% B and hold for one minute, at 62.1 min the percentage of B was set to the initial condition of the run at 2% and hold for about 8 min in order to re-equilibrate the column, for a total run time of 70 min. Mass spectrometry analysis was performed in positive ion mode. The ESI source was used with a voltage of 2.8 kV. The capillary temperature, sheath gas flow, auxiliary gas and spare gas flow were set at 325 °C, 45 arb, 10 arb and 2 respectively. S-lens was set at 70 rf. For the acquisition of spectra, a data-dependent (ddMS2) top 10 scan mode was used. Survey full-scan MS spectra (mass range m/z 381 to 1581) were acquired with resolution R = 70,000 and AGC target 3 × 10^6. MS/MS fragmentation was performed using high-energy c-trap dissociation (HCD) with resolution R = 35,000 and AGC target 1 × 10^6. The normalized collision energy (NCE) was set to 30. The injection volume was 3 μL. The mass spectra analysis was carried out using MaxQuant software (version 1.6.14). MaxQuant parameters were set as follow: trypsin was selected for enzyme specificity; the search parameters were fixed to an initial precursor ion tolerance of 10 ppm and MS/MS tolerance at 20 ppm; as fixed modification, carbamidomethylation was set, whereas oxidation was set as variable modification. The maximum missed cleavages were set to 2. Andromeda search engine searched the spectra in MaxQuant against the Uniprot_CP_Mouse_2018 sequence database. Label free quantification was performed including a match between runs option with the following parameters: protein and peptide false discovery rate was set to 0.01; the quantification was based on the extracted ion chromatograms, with a minimum ratio count of 1; the minimum required peptide length was set to 7 amino acids. Heatmaps were plotted with https://www.bioinformatics.com.cn/srplot, and statistical analyses were performed using MaxQuant software (version 1.6.14) and MetaboAnalyst software (https://www.metaboanalyst.ca/)[61].

High-resolution respirometry

Mitochondrial respiration was measured using a high-resolution respirometer (Oxygraph-2k, Oroboros Instruments) in both cultured myotubes and skeletal muscle tissue. Oxygen consumption was recorded using DatLab7 software, and respiratory states were assessed through substrate–uncoupler–inhibitor titration (SUIT) protocols at 37 °C.

In C2C12 myotubes, oxygen consumption rate (OCR) was measured following the substrate–uncoupler–inhibitor titration (SUIT) protocol SUIT-003_O2_ce_D012, as previously described [56]. At the end of the treatments, C2C12 myotubes were trypsinized, centrifuged at 300 × *g* for 5 min, resuspended in mitochondrial respiration medium MiR05 (0.5 mM EGTA, 3.0 mM $MgCl_2 \cdot 6H_2O$, 60 mM potassium lactobionate, 20 mM taurine, 10 mM KH_2PO_4, 20 mM HEPES, 110 mM sucrose, 1 g/L bovine serum albumin, pH 7.1) and transferred to the chambers of the Oroboros oxygraph. Control and treated samples were assessed simultaneously. After initial stabilization of O_2 flux, 5 mM pyruvate was used to sustain TCA-linked respiration in MiR05 medium. 5 nM oligomycin (Omy), an ATP synthetase inhibitor, was added, and the oxygen consumption was quantified to determine the oligomycin-sensitive and -insensitive respiration. Carbonyl cyanide-p-trifluoromethoxyphenylhydrazone (FCCP), a protonophore and uncoupler of oxidative phosphorylation, was then added at 0.5 µM increments to achieve maximum respiration to quantify the maximum respiratory capacity. This was followed by the inoculation of 500 nM rotenone (Rot) to inhibit complex I of the ETS, and, finally, 2.5 µM antimycin A (Ama), an inhibitor of complex III, was added to determine the non-mitochondrial respiration (ROX). Rates of O_2 consumption (flux) were normalized to total protein content. Briefly, at the end of the experimental procedure, the cellular suspension from the two chambers was centrifuged at 1,000 × *g* for 5 min. The cellular pellet was lysed in 200 µL of lysis buffer (10 mM HEPES, 60 mM KCl, 1 mM EDTA, 0.075% NP40, 1 mM DTT) and then centrifuged at 15,000 × *g* for 15 min at 4 °C. The concentration of the protein in the supernatant was measured with Bradford Reagent.

In freshly dissected muscles, mitochondrial respiration was evaluated by placing the tissue immediately after excision in ice-cold BIOPS solution (50 mM K^+-MES, 20 mM taurine, 0.5 mM DTT, 6.56 mM $MgCl_2$, 5.77 mM ATP, 15 mM phosphocreatine, 20 mM imidazole, 10 mM Ca-EGTA buffer (2.77 mM CaK_2EGTA, 7.23 mM K_2EGTA, pH 7.1) and manually dissected under a stereomicroscope into ~2 mg fiber bundles using fine forceps. Plasma membrane permeabilization was achieved by incubating the bundles in BIOPS supplemented with 50 µg/mL saponin for 20 min on ice with gentle shaking. After permeabilization, fibers were washed in ice-cold BIOPS for 10 min, dried on filter paper, weighed, and transferred to the oxygraph chambers containing MiR05 medium for OCR measurements.

Respiration was recorded using a SUIT protocol SUIT-008_O2_pfi_D014[62,63] in a hyper-oxygenated environment. The following substrates and inhibitors were sequentially added: 1) 1 mM malate, 5 mM pyruvate to determine non-phosphorylating LEAK respiration supported by complex I-linked substrates; 2) 5 mM ADP to achieve maximal phosphorylating respiration from electron input through complex I (CI OXPHOS capacity); 3) 10 µM cytochrome c to assess the integrity of the outer mitochondrial membrane; 4) 10 mM glutamate (CI OXPHOS capacity); 5) 10 mM succinate to saturate complex II and achieve maximal convergent electron flux through complex I and II (CI and CII OXPHOS capacity); 6) 0.5 µM FCCP to assess complex I and II linked maximal capacity (CI and CII ETS capacity); 7) 0.5 µM rotenone to inhibit complex I (CII ETS capacity); and 8) 2.5 M antimycin A to inhibit complex III and obtain the residual oxygen consumption (ROX). Complex IV activity was evaluated after antimycin A, CIII inhibition by ascorbate (0.5 mM) and TMPD (N, N, N', N'-tetramethyl-p-phenylenediamine; 2

mM) injection. At the end, 200 mM azide was adjusted to inhibit CIV. Oxygen fluxes of the different respiratory states were corrected by subtracting residual oxygen consumption following antimycin A treatment and normalized to muscle bundle wet mass.

Mitochondrial content

Total DNA was extracted from myotubes using the NucleoSpin Tissue purification kit (Macherey-Nagel) according to the manufacturer’s instructions. The isolated DNA was eluted in 60 ml of elution buffer. The relative mtDNA amount was expressed as the ratio between the expression of the mitochondrial gene *Cox2* and of the nuclear gene *Rps18*, assessed by real-time PCR analysis using the following TaqMan probes: *Cox2* (Mm03294838_g1) and *Rps18* (Mm00507222_s1).

Alternatively, in muscle slices, mitochondrial content was estimated on the basis of the mean fluorescence of TOM20.

Mitochondrial fragmentation

Mitochondrial morphology was assessed in both C2C12 myotubes and skeletal muscle tissue. Live C2C12 cells were stained with MitoTracker Green FM, washed with PBS, and the images were immediately acquired. Cryosections of muscles were fixed in 4% PFA and immunostained for TOM20. All samples were acquired using a Leica TCS SP8 confocal laser scanning microscope using a 63× immersion objective.

Quantification of mitochondrial fragmentation was performed using the Mitochondria Analyzer plugin for ImageJ[64]. Image pre-processing included Subtract Background, Sigma Filter Plus, and Enhance Local Contrast. Adaptive thresholding was applied using empirically optimized block size and C-value parameters. Post-processing steps (Despeckle and Remove Outliers) were used to refine object segmentation. Finally, the average mitochondrial area was quantified using the plugin’s integrated 2D analysis module.

Mitochondrial membrane potential

Mitochondrial membrane potential in C2C12 myotubes was assessed using JC-1 mitochondrial membrane potential assay kit, according to the manufacturer’s instructions. Briefly, 10 μg/mL JC-1 was added to the culture medium and then mixed gently. Subsequently, cells were incubated in a CO_2 incubator at 37 °C for 15 min. Images were then acquired through a fluorescence microscope (EVOS™ XL Core Imaging System, Thermo Fisher Scientific). Red emission of the dye represented a potential-dependent aggregation of JC-1 in the mitochondria. Conversely, green fluorescence appearing in the cytosol after mitochondrial membrane depolarization represented the monomeric form of JC-1. The average intensity of red and green fluorescence was measured using ImageJ software, and the ratio of JC-1 aggregate (red) to monomer (green) intensity was then calculated.

Reactive Oxygen Species (ROS) production

To measure cellular ROS production, C2C12 myotubes were stained with CellROX R Deep Red Reagent for 30 min at 37 °C and washed with PBS. Images were taken using the EVOS™ XL Core Imaging System, and the mean fluorescence signal intensity was measured using ImageJ. For every experiment assessing cellular oxidative stress, at least three myotubes in each field, five different fields for each replicate, three technical replicates for each treatment were measured.

***Lrp2* silencing**

As previously described[25], at day 3 of differentiation, C2C12 cells were transfected with 50 pmol of *Lrp2* siRNA or siRNA negative control sequence (Ambion, Thermo Fisher Scientific; 4390771) by Lipofectamine 3000 (Invitrogen, Thermo Fisher Scientific) according to the manufacturer's instructions. Myotubes underwent treatments with 50 nM VDBP 24 h later. Transfection of myotubes with Block-iT (Invitrogen, Thermo Fisher Scientific) was used to assess transfection efficiency, which was always >90%. Efficacy of silencing was verified by real-time RT PCR and immunofluorescence.

ELISA

Vitamin D quantification - For in vitro analysis, at the end of treatments, C2C12 myotubes were lysed in sterile physiological saline, and free and total 25-hydroxyvitamin D (25VD) were quantified according to the instructions for the Free 25OH Vitamin D ELISA kit (DIAsource ImmunoAssays) and 25-OH Vitamin D_3 Total ELISA kit (Labor Diagnostika Nord GmbH), respectively.

In vivo, free 25VD was measured in both serum and skeletal muscle samples. Approximately 100 µL of blood were collected from isoflurane-anesthetized mice by submandibular vein puncture and processed according to the kit protocol. Muscle samples were accurately weighed, homogenized in a volume of physiological saline equal to the tissue weight using a tissue homogenizer, and the resulting lysates were directly loaded for ELISA quantification.

VDBP quantification - Approximately 150 µl of blood were collected, serum was diluted 1:80,000, and VDBP serological concentration was measured with the mouse VDBP ELISA Kit PicoKine (Boster Biological Technologies) according to the manufacturer's instructions.

Liquid chromatography-tandem mass spectrometry (LC-MS)

25-hydroxy-vitamin D_3 (25VD) was extracted from 50 µL of serum from WT and *Gc* KO mice with or without LLC tumor (n=5 for each group). Then, 4 µL of a 500 ng/mL methanol solution of the deuterium-labelled internal standard (25-Hydroxyvitamin D3 (6,19,19-d3) solution, Sigma-Aldrich, cat # 739618) were added, followed by protein precipitation using 200 µL of cold methanol. Extraction of 25VD from 30 mg of muscle sample (n=3 for WT and *Gc* KO mice without LLC tumor, and n=5 for each group of tumor-bearing mice) was performed by homogenization (MP Biomedicals FastPrep-24™ 5G) for 3.3 min (5 cycles of 40 s each, speed 6.0 m/s) followed by the addition of 4 µL of a 500 ng/mL methanol solution of the deuterium-labelled internal standard, and by protein precipitation using 200 µL of cold methanol. Both type of samples were then centrifuged (15 min, 4 °C, and 25,155 × *g*), and the supernatant was collected, dried in SpeedVac, and resuspended in 150 µL methanol:H_2O 1:1. Prior to LC-MS analysis, an additional centrifugation step (5 min, 4 °C, 25,155 × *g*) was performed, and the supernatant was transferred to a glass HPLC-vial with an insert and kept at -20 °C until LC-MS analysis.

Samples were vortexed and kept at -20 °C for 20 min to enhance the precipitation. Afterwards, 540 µL of hexane and 60 mL of ethyl acetate were added, and the sample was vortexed for 30 seconds, followed by centrifugation at 21,900 × *g* for 20 min. The supernatant was collected and vacuum-dried. The pellet was then resuspended, prior to the LC-MS analysis, in 50 µL of methanol + 0.1% formic acid and 50 µL of water + 0.1% formic acid. Prior to UHPLC-MS/MS analysis, an additional centrifugation step (5 min, 4 °C, 25,155 × *g*) was performed, and the supernatant was transferred to a glass HPLC vial with an insert and kept at -20 °C until the analysis.

Chromatographic separation of 25VD was achieved on an ACQUITY UPLC CSH C18 column (2.1 × 150 mm, 1.7 µm) using a UHPLC Vanquish system (Thermo Scientific) coupled to a Q-Exactive Plus Hybrid Quadrupole-Orbitrap mass spectrometer (Thermo Scientific). The UHPLC column was operated at 45 °C. A constant flow rate of 0.25 mL/min was applied, with a binary gradient system of high-purity water and 0.1% formic acid (solvent A) and methanol with 0.1% formic acid (solvent B). The initial gradient (50% B) was held for 2 min (0 to 2 min), increased linearly to 100% B over 3 min (2 to 5 min), and held at 100% for 3 min (5 to 8 min) before returning, in 1 min (8 to 9 min), to initial conditions (50% B) for 3 min of column re-equilibration (12.1 to 15 min), resulting in a total run time of 12 min. Injection volume was 5 µL. Thermo Xcalibur software (version 4.1.31.9, Thermo Fisher Scientific) was used to control the instrument, acquire, and process the data.

The eluted analytes were analyzed with the Q-Exactive Plus Hybrid Quadrupole-Orbitrap mass spectrometer (Thermo Scientific), equipped with a heated electrospray ionization source (HESI-II), using the following parameters: capillary temperature, 320 °C; spray voltage, 3,800 V; sheath gas flow, 40 arbitrary units; aux gas flow, 10 arbitrary units. Acquisition was performed in positive ion mode, and data were acquired in Top10 mode (from 100 to 1,000 *m/z*, at a resolution of 70,000 full width at half maximum (FWHM)) and in time-scheduled parallel reaction monitoring (PRM) events to enhance the ion signal intensity. The time schedule for the PRM mode was determined using the start and end times of the 25VD precursor ion in Top10 mode and setting the collision energy to 35 eV in that time range to retain at least 10% of the unfragmented precursor ion. PRM was performed in positive ion mode, at a resolving power of 17,500 FWHM, with automatic gain control (AGC) target: 2×10^5, a maximum injection time of 100 ms, and an isolation window of 4.0 *m/z*.

Identification was carried out by comparing the retention time and fragmentation patterns of the endogenous metabolite with those of the labelled standard before and after its addition. Quantification was performed by comparing the analyte signal to the standard's signal.

Immunoprecipitation

For the whole cell immunoprecipitation assay, cells were lysed in ice-cold HEPES-buffered saline (HBS; 150 mM NaCl, 20 mM HEPES), supplemented with protease inhibitor cocktail. Lysates were stirred at 4 °C for 15 min, centrifuged at 15,000 × *g* for 15 min at 4 °C, and protein concentration was determined by BCA assay. 250 μg of proteins for each sample were incubated for 4 h on a rotatory wheel with the anti-VDBP antibody at RT. The mix containing the antigen-antibody complexes was then incubated with 20 μL of Dynabeads Protein G (Invitrogen, Thermo Fisher Scientific) for 10 min on a rotatory wheel at RT. Immunocomplexes were collected using a magnet, washed twice in HBS and eluted in 30 μL of sample buffer (2% sodium dodecyl sulfate, 150 mM dithiothreitol, and 0.01% bromophenol blue) at 95 °C for 10 min. The interaction between VDBP and actin was evaluated by western blotting.

For the immunoprecipitation of the mitochondrial fraction, cell fractionation was performed with the Mitochondria/Cytosol Fractionation kit (Abcam) according to the manufacturer's instructions, and 200 μg of proteins from the mitochondrial fraction were then subjected to immunoprecipitation as described above.

G-/F-actin ratio

At the end of the indicated treatments, C2C12 myotubes were fixed with 4% PFA for 10 min, permeabilized with 0.1% Triton X-100 for 5 min, washed three times with PBS, and incubated for 2 h at RT with DNase I conjugated with Alexa Fluor 488 (1:500) and Alexa Fluor 633 Phalloidin (1:100) to stain G-actin and F-actin, respectively. After washing with PBS, nuclei were counterstained with DAPI, and images were acquired with a Leica TCS SP8 confocal microscope, using a 63× immersion objective. Quantification of G-/F-actin ratio was performed using ImageJ by measuring the mean fluorescence intensity of the DNase I and Phalloidin fluorescence within individual cells.

In muscles, the G-/F-actin ratio was measured using the G-actin/F-actin In Vivo Assay Kit (Cytoskeleton Inc.) following the manufacturer’s instructions. Briefly, tissues were weighed and homogenized in LAS2 lysis and stabilization buffer. Cell debris was removed by centrifugation at 500 × *g* for 5 min, and the cleared lysates were centrifuged at 100,000 × *g* for 1 hour at 37 °C to separate G-actin (supernatant) from F-actin (pellet). The F-actin pellet was solubilized in depolymerization buffer at a volume equal to that of the G-actin-containing supernatant. Equal volumes of G- and F-actin fractions were resolved by SDS-PAGE and analyzed by Western blotting using the kit-supplied anti-actin antibody. Densitometric analysis was used to calculate the G-/F-actin ratio.

Proximity Ligation Assay

C2C12 cells were plated and differentiated on glass coverslips. At the end of the indicated treatments, a proximity ligation assay (PLA; Duolink, Merck Life Sciences) was performed according to the manufacturer’s instructions. The incubation with the primary antibodies targeting DRP-1 and VDBP was performed ON at 4 °C. At the completion of the PLA, immunofluorescent staining of MyHC was performed.

Animal experiments

Animal experiments are reported in accordance with the ARRIVE guidelines. All procedures were approved by the Institutional Animal Care and Use Committee at the University of Piemonte Orientale and were authorized after ministerial clearance (Italian Ministero della Salute, Authorization n. DB064.25). Animal welfare was monitored by trained personnel, and all adverse events were promptly reported with appropriate actions taken. Euthanasia was performed according to institutional and national guidelines using cervical dislocation at the planned endpoint or earlier if humane endpoints were reached. C57BL/6J mice were from the breeding colony maintained in our animal facility while the VDBP-null (*Gc* KO) mice, with a systemic lack of VDBP, were from the Stony Brook University, New York, and then bred in our animal facility. Three-month old male mice, weight-matched, were used for all experiments. Animals were fed ad libitum with a standard chow (Envigo Tekland 2014) and had unrestricted access to drinking water. The light/dark cycle in the room consisted of 12/12 hours with artificial light. Invasive procedures (cancer cells inoculation and intramuscular VDBP injection) were performed under inhalation of isoflurane in medical oxygen. Intramuscular administrations in the tibialis anterior of 1.5 mg/kg VDBP (right limb) or saline (left limb) in *Gc* KO mice were performed of every 48 h. At the experimental endpoints, animals were killed through cervical dislocation, and tissues used for the study were immediately excised, weighted, and processed or stored for further analysis.

To induce tumor-associated muscle wasting, 10^6 LLC cells resuspended in 100 µl of saline were injected in the back of mice[65]. Controls were injected with the same volume of saline. Food intake was measured every 5 days. After 23 days from the injection, animals were killed, and blood and tissues were harvested.

Sample sizes for VDBP injection experiments in *Gc* KO mice were power-calculated (α=0.05, 80% power) using preliminary TA weight data from our laboratory (mean 51.39 mg, SD 3.61), yielding n=8/group to detect a ≥10% difference between injected and non-injected mice. For cachexia experiments, sample size was determined based on a previous LLC-cachexia model studies [31,65].

Grip strength test

To measure in vivo limb force, mice were suspended by the tail and allowed to grasp a grid with either one hind limb or both, depending on the experiment. A force transducer attached to the grid measured the peak force. The final value is the average of 5 repeated force measurements. The test was performed immediately before the treatments and repeated as indicated in each experiment.

Treadmill exhaustion test

Muscle performance was evaluated using a treadmill-based exhaustion protocol. Before the test, mice were acclimated to the treadmill (Panlab Harvard Apparatus; LE8710M) with a 10-min run at a constant speed of 14 cm/s once per day for two alternate days. The day of the experiment, each mouse was placed into an exercise test regimen of 14 cm/s for 10 min. The speed was then increased by 2 cm/s every 2 min, up to a maximum of 46 cm/s, which was maintained until exhaustion, defined as the inability to continue running despite repeated electrical stimuli. At that moment, total running time and distance were recorded.

Glucose and insulin tolerance tests

Glucose and insulin tolerance tests were performed to evaluate systemic glucose metabolism and insulin sensitivity. For the glucose tolerance test (GTT), mice were fasted overnight and injected intraperitoneally (i.p.) with D-glucose (1.5 g/kg body weight; BDH Laboratory Supplies) dissolved in sterile saline. For the insulin tolerance test (ITT), conducted 7 days apart from the GTT, mice were fasted for 6 hours and injected i.p. with human recombinant insulin (0.75 IU/kg body weight; Actrapid, Novo Nordisk) diluted in sterile saline (0.25 IU/mL). Blood glucose levels were measured from the tail vein at baseline (t=0) and at 15, 30, 60, and 120 min after injection using the OneTouch Verio Reflect glucometer (Lifescan).

Indirect calorimetry

Mice were individually housed in metabolic cages (Oxylet LE 1305 Physiocage, Panlab, Harvard Apparatus, Barcelona, Spain). After a 24-hour acclimatation period, data were recorded continuously for 24 hours under controlled environmental conditions (22 °C, 12-hour light/dark cycle), with ad libitum access to food and water. Oxygen consumption (VO_2) and carbon dioxide production (VCO_2) were measured every 15 min using the Oxylet LE405 gas analyzer (Panlab) with a constant airflow rate of 900 mL/min (Oxylet LE400 air supplier, Panlab). Respiratory quotient (RQ; VCO_2/VO_2) and energy expenditure (EE) were calculated using Metabolism v3.0.01 software.

Histological analysis and immunofluorescence

Muscles were excised, weighted, mounted in Killik embedding medium (Bio Optica Milano SpA), frozen in liquid-nitrogen-cooled isopentane, and stored at -80 °C. Transversal muscle sections (7 μm) were cryo-sectioned from the middle part of each muscle. Slices were fixed in 4% PFA for 20 min, washed, permeabilized with 0.2% Triton X-100 in 1% BSA for 15 min, and blocked with 4% BSA for 30 min. Myofiber cross sectional areas (CSA) and mitochondrial morphology were determined by immunofluorescence with anti-laminin and anti-TOM20, respectively. 24 hours of incubation with the specific primary antibodies at 4 °C ON were followed by PBS washing and 45 min of Alexa Fluor anti-rabbit 488 secondary antibody at RT. Nuclei were counterstained with DAPI. Eventually, sections were washed in PBS and cover slipped using SlowFade Gold antifade reagent (Invitrogen, Thermo Fischer Scientific) mounting medium. Images of whole muscle sections were acquired with the slide scanner Pannoramic Midi 1.14 (3DHISTECH Kft) and CSA of fibers quantified with ImageJ software. Myofiber type distribution and respective CSA was obtained by immunofluorescence for myosin type IIa, IIb, and laminin. Briefly, after cutting, slices were directly blocked with 3% BSA for one hour without fixing, washed, and probed with the anti-MyHC Type IIa, anti-MyHC Type IIb, and anti-laminin primary for 1 hour at RT. After PBS washing, sections were incubated with the appropriate Alexa Fluor-conjugated secondary antibodies. Type IIx fibers were defined as double negative. Images were acquired using a Leica TCS SP8 confocal microscope and analyzed using ImageJ software. To perform CSA quantification of the different myosin isoforms, laminin-stained images were optimized by enhancing contrast, applying Gaussian blur and despeckling, and subtracting background. Myofiber boundaries were segmented by the plugin "MorphoLibJ"[66]. Fiber areas were counted and measured with the command "analyze particles". Then CSA segmentation was applied to the other images of the different myosin isoforms.

NMJ visualization and analysis

Immunofluorescence analysis of the NMJs was performed in extensor digitorum longus (EDL). Freshly dissected EDL muscles were fixed with 4% PFA for 10 min and stored in PBS until time of processing. Myofibers were manually dissociated with forceps and washed three times with PBS for 30 min. Post-synaptic AChRs were labelled with α-bungarotoxin (α-BTX; 1:500). Muscles were permeabilized in 2% Triton X-100 in PBS for 90 min then blocked in 4% BSA and 1% Triton X-100 in PBS for 60 min. Samples were incubated at 4 °C ON in blocking solution containing the primary anti-neurofilament antibody. The following day, muscles were washed three times with PBS for 30 min and incubated with the Alexa Fluor anti-chicken 546 secondary antibody. Samples were washed three more times with PBS for 30 min and whole-mounted with Mowiol. Images were captured using a Leica TCS SP8 confocal microscope. A 20× objective was used to measure AChR cluster and endplate areas, while a 63× immersion objective was used to determine NMJ denervation. Confocal Z-stacks were acquired identifying the upper limits of the Z-stack using the neurofilament (NF-1) labeling and the lower limit through the postsynaptic staining (α-BTX). All analyses were performed on maximum intensity Z-stack projections. The AChR and endplate areas were determined using ImageJ software. To quantify NMJ denervation ImageJ software combined with the NMJ-morph workflow[67] was used.

RNA-seq

Total RNA was extracted from about 20 mg of fresh gastrocnemii from LLC-bearing WT and *Gc* KO mice (N=7 and N=6, respectively) and their saline-injected littermates (N=3 for each group) using the Reliaprep RNA tissue miniprep system kit (Promega). RNA quality was assessed on an Agilent RNA 6000 Nano (Agilent Technologies, Inc.), and only samples with high RNA integrity number (RIN > 8) were used for subsequent library preparation. Paired-end cDNA libraries were prepared for each sample using the Illumina TruSeq RNA Sample Preparation Kit following the manufacturer's procedures. Library quality was checked on an Agilent High Sensitivity DNA Kit by Agilent Bioanalyzer 2100 (Agilent). Libraries were multiplexed, clustered, and sequenced on an Illumina NovaSeq 6000. Library construction and RNA-seq were performed at the IEO European Institute of Oncology in Milan, Italy.

Good quality of RNA-Seq Sequencing has been investigated using FastQC software on raw reads (http://www.bioinformatics.babraham.ac.uk/projects/fastqc/). After quality check, raw reads were mapped to the mouse reference genome GRCm38/mm10 using STAR aligner[68] and gene quantification has been performed using RSEM software[69]. Genes were considered expressed if they present a TPM>1 in at least one sample. Differentially expressed genes has been calculated using DESeq2[70] with the following thresholds: |log2FC|>1.5 and FDR<0.1.

Heatmaps of unsupervised hierarchical clustering of DEGs have been performed using pheatmap R package.

The list of DEGs in each comparison has been analyzed using IPA Ingenuity Pathway Analysis software (QIAGEN Srl, https://www.qiagen.com/us/products/discovery-and-translational-research/next-generation-sequencing/informatics-and-data/interpretation-content-databases/ingenuity-pathway-analysis/).

Gene Set Enriched Analysis[71] has been performed using the desktop application on the dataset “Mouse ortholog hallmark gene sets” with default parameters; GSEA Terms have been selected using the following thresholds: |NES|>1 and FDR <0.1.

Statistical Analysis

The investigators quantifying the experimental outcomes were blind to the treatments, and the statistic evaluation of the experimental data was performed by another investigator not directly involved in data collection and parameter measurement. Continuous data are presented as the mean ± SEM. Outliers in the measurements were identified by mean of the interquartile range (IQR), as either below Q1 - 1.5 IQR or above Q3 + 1.5 IQR and excluded from the analysis. The differences among independent groups in continuous data such as myotube diameters, relative mRNA expression or force were evaluated using Student’s t-test or one-way ANOVA test followed by Tukey’s multiple comparisons test, which were conducted upon verification of the normality assumption using the Kolmogorov-Smirnov test (where applicable). Differences in the CSA distribution between groups were assessed using a chi-square goodness-of-fit test. Statistical significance was assumed for $P < 0.05$. Unless otherwise specified, statistical analyses were performed with GraphPad Prism 10.4.0 (GraphPad Software).

Data Availability

Proteomic data are available via ProteomeXchange with the identifier PXD042024 [https://www.ebi.ac.uk/pride/archive/projects/PXD042024].

The RNA-Seq data are available in the NCBI GEO with the ID GSE231768 [https://www.ncbi.nlm.nih.gov/geo/query/acc.cgi?acc=GSE231768].

Source data are provided with this paper.

References

1. Otterbein, L. R., Cosio, C., Graceffa, P. & Dominguez, R. Crystal structures of the vitamin D-binding protein and its complex with actin: Structural basis of the actin-scavenger system. *Proceedings of the National Academy of Sciences* 99, 8003–8008 (2002).
2. Meier, U., Gressner, O., Lammert, F. & Gressner, A. M. Gc-Globulin: Roles in Response to Injury. *Clin Chem* 52, 1247–1253 (2006).
3. Kew, R. R., Tabrizian, T., Vosswinkel, J. A., Davis, J. E. & Jawa, R. S. Vitamin D–binding protein deficiency in mice decreases systemic and select tissue levels of inflammatory cytokines in a murine model of acute muscle injury. *Journal of Trauma and Acute Care Surgery* 84, 847–854 (2018).
4. Dahl, B. *et al.* Gc-globulin is an acute phase reactant and an indicator of muscle injury after spinal surgery. *Inflamm Res* 50, 39–43 (2001).
5. Kew, R. R. The Vitamin D Binding Protein and Inflammatory Injury: A Mediator or Sentinel of Tissue Damage? *Front Endocrinol (Lausanne)* 10, 470 (2019).

6. Trujillo, G. *et al.* Neutrophil Recruitment to the Lung in Both C5a- and CXCL1-Induced Alveolitis Is Impaired in Vitamin D–Binding Protein–Deficient Mice. *The Journal of Immunology* 191, 848–856 (2013).

7. Mull, B. *et al.* Differential expression of Vitamin D binding protein in thyroid cancer health disparities. *Oncotarget* 12, 596–607 (2021).

8. Huang, Y. F. *et al.* Vitamin D–binding protein enhances epithelial ovarian cancer progression by regulating the insulin-like growth factor-1/akt pathway and Vitamin D receptor transcription. *Clinical Cancer Research* 24, 3217–3228 (2018).

9. Kratzer, T. B., Weinstein, S. J., Albanes, D. & Mondul, A. M. Vitamin D binding protein and risk of renal cell carcinoma in the prostate, lung, colorectal and ovarian cancer screening trial. *Int J Cancer* 147, 669–674 (2020).

10. Bijian, K. *et al.* Serum proteomic approach for the identification of serum biomarkers contributed by oral squamous cell carcinoma and host tissue microenvironment. *J Proteome Res* 8, 2173–2185 (2009).

11. Timms, J. F. *et al.* Discovery of serum biomarkers of ovarian cancer using complementary proteomic profiling strategies. *Proteomics Clin Appl* 8, 982–993 (2014).

12. Pawlik, T. M. *et al.* Proteomic analysis of nipple aspirate fluid from women with early-stage breast cancer using isotope-coded affinity tags and tandem mass spectrometry reveals differential expression of vitamin D binding protein. *BMC Cancer* 6, 68 (2006).

13. Mak, R. H., Querfeld, U., Gonzalez, A., Gunta, S. & Cheung, W. W. Differential effects of 25-hydroxyvitamin d3 versus 1α 25-dihydroxyvitamin d3 on adipose tissue browning in ckd-associated cachexia. *Cells* 10, 1–22 (2021).

14. Kalousova, M. *et al.* Vitamin D Binding Protein Is Not Involved in Vitamin D Deficiency in Patients with Chronic Kidney Disease. *Biomed Res Int* 2015, 492365 (2015).

15. Cho, E.-H. *et al.* The discovery of biomarkers for type 2 diabetic nephropathy by serum proteome analysis. *Proteomics Clin Appl* 1, 352–361 (2007).
16. Rinaldi, A. *et al.* Increased Circulating Levels of Vitamin D Binding Protein in MS Patients. *Toxins (Basel)* 7, 129–137 (2015).
17. Chelliah, S. S., Bhuvanendran, S., Magalingam, K. B., Kamarudin, M. N. A. & Radhakrishnan, A. K. Identification of blood-based biomarkers for diagnosis and prognosis of Parkinson’s disease: A systematic review of proteomics studies. *Ageing Res Rev* 73, 101514 (2022).
18. Metcalf, J. P. *et al.* Gcglobulin functions as a cochemotaxin in the lower respiratory tract. A potential mechanism for lung neutrophil recruitment in cigarette smokers. *Am Rev Respir Dis* 143, 844–849 (1991).
19. Sartori, R., Romanello, V. & Sandri, M. Mechanisms of muscle atrophy and hypertrophy: implications in health and disease. *Nat Commun* 12, 1–12 (2021).
20. Baccam, A. *et al.* The Mechanical Stimulation of Myotubes Counteracts the Effects of Tumor-Derived Factors Through the Modulation of the Activin/Follistatin Ratio. *Front Physiol* 10, 401 (2019).
21. Hanna, R. A. *et al.* Microtubule-associated Protein 1 Light Chain 3 (LC3) Interacts with Bnip3 Protein to Selectively Remove Endoplasmic Reticulum and Mitochondria via Autophagy. *Journal of Biological Chemistry* 287, 19094–19104 (2012).
22. Li, G.-B. *et al.* Mitochondrial fission and mitophagy depend on cofilin-mediated actin depolymerization activity at the mitochondrial fission site. *Oncogene* 37, 1485–1502 (2018).

23. Matsuda, N. *et al.* PINK1 stabilized by mitochondrial depolarization recruits Parkin to damaged mitochondria and activates latent Parkin for mitophagy. *Journal of Cell Biology* 189, 211–221 (2010).

24. Abboud, M. *et al.* Evidence for a specific uptake and retention mechanism for 25-hydroxyvitamin D (25OHD) in skeletal muscle cells. *Endocrinology* 154, 3022–3030 (2013).

25. Sustova, H. *et al.* Opposing effects of 25-hydroxy- and 1α,25-dihydroxy-vitamin D 3 on pro-cachectic cytokine-and cancer conditioned medium-induced atrophy in C2C12 myotubes. *Acta Physiologica* 226, e13269 (2019).

26. Moore, A. S., Wong, Y. C., Simpson, C. L. & Holzbaur, E. L. F. Dynamic actin cycling through mitochondrial subpopulations locally regulates the fission–fusion balance within mitochondrial networks. *Nature Communications 2016 7:1* 7, 1–13 (2016).

27. Sheikh-Hamad, D., Holliday, M. & Li, Q. Megalin-Mediated Trafficking of Mitochondrial Intracrines: Relevance to Signaling and Metabolism. *Journal of Cellular Immunology,; Volume 3(Issue 6):364-369* Volume 3, 364–369 (2021).

28. Cassidy-Stone, A. *et al.* Chemical Inhibition of the Mitochondrial Division Dynamin Reveals Its Role in Bax/Bak-Dependent Mitochondrial Outer Membrane Permeabilization. *Dev Cell* 14, 193–204 (2008).

29. Mao, X. *et al.* Phosphorylation of Dynamin-Related Protein 1 (DRP1) Regulates Mitochondrial Dynamics and Skeletal Muscle Wasting in Cancer Cachexia. *Front Cell Dev Biol* Volume 9-, (2021).

30. Camperi, A. *et al.* Vitamin D and VDR in cancer cachexia and muscle regeneration. *Oncotarget* 8, 21778–21793 (2017).

31. Safadi, F. F. *et al.* Osteopathy and resistance to vitamin D toxicity in mice null for vitamin D binding protein. *Journal of Clinical Investigation* 103, 239–251 (1999).

32. Viloria, K. *et al.* Vitamin-D-Binding Protein Contributes to the Maintenance of α Cell Function and Glucagon Secretion. *Cell Rep* 31, (2020).

33. Lee, D. & Goldberg, A. L. SIRT1 protein, by blocking the activities of transcription factors FoxO1 and FoxO3, inhibits muscle atrophy and promotes muscle growth. *J Biol Chem* 288, 30515–30526 (2013).

34. Bouillon, R., Schuit, F., Antonio, L. & Rastinejad, F. Vitamin D Binding Protein: A Historic Overview. *Front Endocrinol (Lausanne)* 10, 1–21 (2020).

35. Lahoute, C. *et al.* Premature Aging in Skeletal Muscle Lacking Serum Response Factor. *PLoS One* 3, e3910 (2008).

36. Cenik, B. K. *et al.* Myocardin-related transcription factors are required for skeletal muscle development. *Development* 143, 2853–2861 (2016).

37. Coletti, D., Daou, N., Hassani, M., Li, Z. & Parlakian, A. Serum Response Factor in muscle tissues: from development to ageing. *Eur J Transl Myol* 26, (2016).

38. Sakuma, K., Akiho, M., Nakashima, H., Akima, H. & Yasuhara, M. Age-related reductions in expression of serum response factor and myocardin-related transcription factor A in mouse skeletal muscles. *Biochimica et Biophysica Acta (BBA) - Molecular Basis of Disease* 1782, 453–461 (2008).

39. Collard, L. *et al.* Nuclear actin and myocardin-related transcription factors control disuse muscle atrophy through regulation of Srf activity. *J Cell Sci* 127, 5157–5163 (2014).

40. Rehklau, K. *et al.* Cofilin1-dependent actin dynamics control DRP1-mediated mitochondrial fission. *Cell Death Dis* 8, 1–12 (2017).

41. Korobova, F., Ramabhadran, V. & Higgs, H. N. An actin-dependent step in mitochondrial fission mediated by the ER-associated formin INF2. *Science* 339, 464–7 (2013).
42. Dev, R. *et al.* Preliminary Report: Vitamin D Deficiency in Advanced Cancer Patients with Symptoms of Fatigue or Anorexia. *Oncologist* 16, 1637–1641 (2011).
43. Dai, Z., Luo, X., Xie, H. & Peng, H. B. The Actin-Driven Movement and Formation of Acetylcholine Receptor Clusters. *Journal of Cell Biology* 150, 1321–1334 (2000).
44. Blunk, A. D. *et al.* Postsynaptic actin regulates active zone spacing and glutamate receptor apposition at the Drosophila neuromuscular junction. *Molecular and Cellular Neuroscience* 61, 241–254 (2014).
45. Mallik, B. & Frank, C. A. Roles for Mitochondrial Complex I Subunits in Regulating Synaptic Transmission and Growth. *Front Neurosci* 16, 846425 (2022).
46. Ahn, B. *et al.* Mitochondrial oxidative stress impairs contractile function but paradoxically increases muscle mass via fibre branching. *J Cachexia Sarcopenia Muscle* 10, 411–428 (2019).
47. Sartori, R. *et al.* Perturbed BMP signaling and denervation promote muscle wasting in cancer cachexia. *Sci Transl Med* 13, (2021).
48. Daou, N. *et al.* Displaced myonuclei in cancer cachexia suggest altered innervation. *Int J Mol Sci* 21, 1–17 (2020).
49. Huot, J. R., Pin, F. & Bonetto, A. Muscle weakness caused by cancer and chemotherapy is associated with loss of motor unit connectivity. *Am J Cancer Res* 11, 2990 (2021).
50. Hunt, L. C. *et al.* Integrated genomic and proteomic analyses identify stimulus-dependent molecular changes associated with distinct modes of skeletal muscle atrophy. *Cell Rep* 37, 109971 (2021).

51. Penafuerte, C. A. *et al.* Identification of neutrophil-derived proteases and angiotensin II as biomarkers of cancer cachexia. *British Journal of Cancer 2016 114:6* 114, 680–687 (2016).

52. McLoughlin, T. J., Tsivitse, S. K., Edwards, J. A., Aiken, B. A. & Pizza, F. X. Deferoxamine reduces and nitric oxide synthase inhibition increases neutrophil-mediated myotube injury. *Cell Tissue Res* 313, 313–9 (2003).

53. Judge, S. M. *et al.* Skeletal Muscle Fibrosis in Pancreatic Cancer Patients with Respect to Survival. *JNCI Cancer Spectr* 2, (2018).

54. Fuster, G. *et al.* Are Peroxisome Proliferator-Activated Receptors Involved in Skeletal Muscle Wasting during Experimental Cancer Cachexia? Role of β2-Adrenergic Agonists. *Cancer Res* 67, 6512–6519 (2007).

55. Luo, Y. *et al.* Cancer usurps skeletal muscle as an energy repository. *Cancer Res* 74, 330–340 (2014).

56. Raiteri, T. *et al.* The Atrophic Effect of 1,25(OH)2 Vitamin D3 (Calcitriol) on C2C12 Myotubes Depends on Oxidative Stress. *Antioxidants* 10, 1980 (2021).

57. Reano, S. *et al.* Unacylated Ghrelin Enhances Satellite Cell Function and Relieves the Dystrophic Phenotype in Duchenne Muscular Dystrophy mdx Model. *Stem Cells* 35, 1733–1746 (2017).

58. Filigheddu, N. *et al.* Ghrelin and Des-Acyl Ghrelin Promote Differentiation and Fusion of C2C12 Skeletal Muscle Cells. *Mol Biol Cell* 18, 986–994 (2007).

59. Bolte, S. & Cordelières, F. P. A guided tour into subcellular colocalization analysis in light microscopy. *J Microsc* 224, 213–232 (2006).

60. Martinotti, S. *et al.* HMGB1 Osteo-Modulatory Action on Osteosarcoma SaOS-2 Cell Line: An Integrated Study From Biochemical and -Omics Approaches. *J Cell Biochem* 117, 2559–69 (2016).

61. Manfredi, M., Martinotti, S., Gosetti, F., Ranzato, E. & Marengo, E. The secretome signature of malignant mesothelioma cell lines. *J Proteomics* 145, 3–10 (2016).

62. Lemieux, H., Blier, P. U. & Gnaiger, E. Remodeling pathway control of mitochondrial respiratory capacity by temperature in mouse heart: electron flow through the Q-junction in permeabilized fibers. *Sci Rep* 7, 2840 (2017).

63. Holmström, M. H., Iglesias-Gutierrez, E., Zierath, J. R. & Garcia-Roves, P. M. Tissue-specific control of mitochondrial respiration in obesity-related insulin resistance and diabetes. *American Journal of Physiology-Endocrinology and Metabolism* 302, E731–E739 (2012).

64. Chaudhry, A., Shi, R. & Luciani, D. S. A pipeline for multidimensional confocal analysis of mitochondrial morphology, function, and dynamics in pancreatic β-cells. *American Journal of Physiology-Endocrinology and Metabolism* 318, E87–E101 (2019).

65. Zhang, G. *et al.* Tumor induces muscle wasting in mice through releasing extracellular Hsp70 and Hsp90. *Nat Commun* 8, 589 (2017).

66. Legland, D., Arganda-Carreras, I. & Andrey, P. MorphoLibJ: integrated library and plugins for mathematical morphology with ImageJ. *Bioinformatics* 32, 3532–3534 (2016).

67. Jones, R. A. *et al.* NMJ-morph reveals principal components of synaptic morphology influencing structure–function relationships at the neuromuscular junction. *Open Biol* 6, 160240 (2016).

68. Dobin, A. *et al.* STAR: ultrafast universal RNA-seq aligner. *Bioinformatics* 29, 15–21 (2013).

69. Li, B. & Dewey, C. N. RSEM: Accurate transcript quantification from RNA-Seq data with or without a reference genome. *BMC Bioinformatics* 12, 1–16 (2011).

70. Love, M. I., Huber, W. & Anders, S. Moderated estimation of fold change and dispersion for RNA-seq data with DESeq2. *Genome Biol* 15, 550 (2014).

71. Subramanian, A. *et al.* Gene set enrichment analysis: A knowledge-based approach for interpreting genome-wide expression profiles. *Proc Natl Acad Sci U S A* 102, 15545–15550 (2005).

Acknowledgements

We would like to express our thanks to Maraiza Alves Teixeira, Marilisa De Feudis, Emanuela Agosti, and Hana Sustova, past members of the laboratory, for their participation in the initial steps of this work. We also thank Stefania Raimondo and Myriam Hsu (University of Torino) and Lorena Zentilin (International Centre for Genetic Engineering and Biotechnology (ICGEB), Trieste, Italy) for their early support and for providing reagents during the initial phase of the project.

We are grateful to Said Hashemolhosseini (Friedrich-Alexander Universität, Erlangen-Nürnberg, Germany) and Daniela Talarico (San Raffaele Scientific Institute, Milan, Italy) for sharing their techniques for characterizing NMJs in vitro and in vivo.

Finally, a special thank you to Elia Angelino (University of Torino), Hajar Meskine, and Marco Varalda (University of Piemonte Orientale) for their suggestions and scientific support in many experiments.

We thank the "Advanced Microscopy", "Metabolism", "Metabolomics & Proteomics", and "Bioinformatics" facilities of the UPO Interdepartmental Center "Ipazia" for their support with image acquisition, mitochondrial respiration measurements, proteome identification, and RNA-seq analysis.

We acknowledge the Italian Ministry of University and Research (MUR) programs “Departments of Excellence 2023–2027” (Department of Translational Medicine, Università del Piemonte Orientale) and the Project Age-It, which has received funding from the MUR – M4C2 1.3 of PNRR, funded by the European Union - NextGenerationEU (Grant agreement no. PE_00000015 - CUP: C13C22000660001); PRIN-2022-PNRR "WESTERNAGE” (P2022Z4EB5) and PRIN MISS.GO project (2022ALX9ZM) to F.P.; PRIN-2022 (WFXCWM-A) to P.E.P.; PRIN-2022 (9CJ27R) and PRIN-2022-PNRR (P2022AFS8P) to D.C.; and the Italian Association for Cancer Research (AIRC, Investigator Grant ID: 27014) to G.P. T.R is a recipient of a Young Research grant from Fondazione Cariplo (ID: 2025-1174).

Author Contributions

N.F., T.R., P.E.P., and F.P. conceived the work and supervised the experiments; T.R., A.S., I.Z., A.A., M.M., S.F., F.F., and S.R. performed the experiments; R.R.K. and G.P. provided essential resources; L.S., D.C., F.F., and F.P. performed bioinformatic and statistical analyses; N.F., T.R., and S.R. wrote the manuscript. All authors reviewed and edited the manuscript.

Competing interests

F.P. received fees for providing educational sessions from Abiogen and Menarini.

The other authors have no competing interests.

Figure Legends

Figure 1. VDBP induces atrophy in C2C12 myotubes and enhances mitophagy. (**A**) Myotube diameters were measured after a 24-h treatment with 10, 50, or 100 nM VDBP; n=3 independent experiments. Scale bar 100 µm. (**B**) Diameters of myofibers from EDL muscle were measured after 24 h treatment with 50 nM VDBP. Each dot represents a single EDL myofiber from a single muscle; n=26 (NT) and 24 (VDBP). Scale bar 200 µm. (**C**) The expression of atrogenes *Fbxo32* and *Trim63* was assessed by real-time RT-PCR, using *Gusb* as the housekeeping gene; n=3 independent experiments. (**D**) C2C12 myotubes were treated with 50 nM VDBP with or without the proteasome inhibitor MG-132 (10 μM). Dexamethasone (DEXA, 5 μM) was used as a positive control of UPS-mediated atrophy. Myotube diameters were measured after 24 h of treatment; n=4 independent experiments. (**E**) Fusion index after 72 h of VDBP treatment; n=9, with each dot representing an experimental replicate from three independent experiments. (**F**) Autophagic flux was assessed by Western blot analysis of LC3B II accumulation with and without 10 µM chloroquine (CLQ). The bars are the average ratios of LC3B II/LC3B I with CLQ and LC3B II/LC3B I without CLQ, normalized to the signals from untreated cells; n=4 independent experiments. (**G**) The expression of the autophagy-related genes *Ctsl*, *Gabarap*, *Atg12*, and *Bnip3* was assessed by real-time RT-PCR; n=3 three independent experiments. (**H**) To assess mitophagy, C2C12 myotubes were treated for 24 h with 50 nM VDBP, and colocalization of mitochondria (MitoTracker™ Green FM) with lysosomes (LysoTracker™ Red DND-99) was evaluated with the JACoP plugin for ImageJ and expressed as Pearson's coefficient; n=6 independent experiments. Scale bar 20 µm. (**I**) Cytosolic (Cyto) and mitochondrial (Mito) fractions from VDBP-treated myotubes were analyzed by western

blotting. VDAC was used as a mitochondrial fraction marker. The relative intensity of the mitochondrial LC3B II was normalized to VDAC; n=3 independent experiments. All treatments were in serum-free medium. Data are presented as means ± SEM. Statistical analysis: one-way ANOVA followed by Tukey's multiple comparisons test for (A) and (D); two-tailed unpaired t-test for (B), (C), and (E)-(I). Source data are provided as a Source Data file.

Figure 2. VDBP treatment affects myotube proteome. (**A-B)** C2C12 myotubes were treated with VDBP for 18 h; n=3 biological replicates for each condition. (**A**) Hierarchical clustering heatmap of the top 50 deregulated proteins. (**B**) Bar graph of Log_{10} fold change of statistically significant proteins ($p< 0.05$). (**C-D**) The proteome of C2C12 myotubes was assessed after 24 h of treatment with VDBP; n=4 biological replicates for each condition. (**C**) Hierarchical clustering heatmap of the top 50 deregulated proteins. (**D**) Bar graph of proteins with $|\text{Log}_{10}$ fold change$| \geq 0.2$ and $p< 0.05$. White bars represent proteins related to actin, while the black ones denote proteins related to metabolism. Statistical analysis: Peptides with FDR lower than 1.0% underwent two-tailed unpaired t-test. Source data are provided in Supplementary Data 1 (18 h) and Supplementary Data 2 (24 h), and available via ProteomeXchange.

Figure 3. VDBP induces mitochondrial dysfunction in C2C12 myotubes. (**A**) Representative oxygen consumption rate (OCR) of C2C12 myotubes after 24 h treatment with 50 nM VDBP. (**B**) Mitochondrial respiration (specific oxygen flux in the routine state, leakage [LEAK] state, and maximal respiratory capacity [ET]) in intact C2C12 myotubes was assessed with an Oroboros 2K high-resolution respirometer through a substrate, uncoupler, inhibitor, titration (SUIT) protocol. (**C**) ATP-linked respiration. (**D**) Reserve respiratory capacity. (B)-(D) n=3 independent experiments. (**E**) Mitochondrial DNA content in C2C12 myotubes was quantified

by measuring, by real-time RT-PCR, the expression of the mitochondrial gene *Cox2* (mtDNA) normalized on the genomic gene *Rps18* (nDNA); n=12 experimental replicates from 4 independent experiments. (**F-G**) The expression of (**F**) mitochondria biogenesis marker *Ppargc1a* and (**G**) mitochondrial dynamic markers *Opa1* (fusion) and *Mff* (fission) was assessed by real-time RT-PCR using *Gusb* as the housekeeping gene; n=3 independent experiments. (**H**) Mitochondrial morphology analysis of VDBP-treated C2C12 myotubes was performed using Mitochondria Analyzer plugin for ImageJ. Bar graph represents the mean mitochondrial in control and VDBP-treated myotubes; n=6 independent experiments. Scale bar 20 µm. (**I**) Mitochondrial membrane potential depolarization was evaluated by JC-1 staining after 24 h of treatment. Bars represent the quantification of the ratio of red/green fluorescence, indicative of membrane polarization; n=7 (NT) and 9 (VDBP) experimental replicates from three independent experiments. Scale bar 100 µm. (**J**) C2C12 myotubes were treated with VDBP with or without 10 µM mitoTEMPO. ROS production was evaluated by CellROX Deep Red reagent and quantified as the fluorescence mean intensity of each myotube; n=6 experimental replicates from three independent experiments. Scale bar 100 µm. (**K**) Myotube diameters were measured after 24 h treatment with VDBP in the presence or absence of mitoTEMPO; n=3 independent experiments. (**L**) Mitochondrial membrane potential was evaluated in the presence of mitoTEMPO; n=5 experimental replicates from three independent experiments. All treatments were in serum-free medium. Data are presented as means ± SEM. Statistical analysis: two-tailed unpaired t-test for (B)-(I); one-way ANOVA followed by Tukey's multiple comparisons test for (J)-(L). Source data are provided as a Source Data file.

Figure 4. VDBP enters C2C12 cells via megalin and induces atrophy independently of vitamin D by perturbing intracellular actin dynamics. (**A-C**) C2C12 myotubes were

transfected with 50 pmol of non-targeting siRNA (NT) or siRNA targeting megalin (*Lrp2*); 24 h post-silencing, myotubes were treated with 50 nM VDBP for 24 h, and (**A**) intracellular VDBP internalization in C2C12 myotubes was evaluated by Western blotting; n=4 (siRNA NT) and 3 (siRNA *Lrp2*) experimental replicates from four independent experiments. (**B**) ROS production was evaluated by CellROX Deep Red reagent and quantified as fluorescence mean intensity of each myotube; n=4 experimental replicates from two independent experiments. (**C**) Myotube diameters were measured from n=3 independent experiments. (**D-F**) C2C12 myotubes were treated for 24 h with VDBP, 25-hydroxy-vitamin D_3 (25VD), or VDBP pre-bound to 25VD in a 1:1 stoichiometric ratio. At the end of treatment, (**D**) ROS production was measured; n=6 experimental replicates from three independent experiments. (**E**) Myotube diameters measured from n=3 independent experiments. (**F**) Intracellular levels of free and total 25VD were assessed by specific ELISAs; n=3 experimental replicates. (**G**) Immunoprecipitation (IP) of VDBP was performed in whole cell lysates of C2C12 myotubes after 24 h of treatment with 50 nM VDBP. The interaction between VDBP and actin was analyzed by western blotting; representative image of n=3 independent experiments. (**H**) Perturbation of actin dynamics after treatment with VDBP was assessed as the ratio between G-actin (stained with Alexa Fluor-conjugated DNase I) and F-actin (visualized by phalloidin staining); n=6 experimental replicates from three independent experiments. Scale bar 20 μm. (**I-K**) C2C12 myotubes were pre-treated with 250 nM jasplakinolide (Jas) for 30 min before the 24 h-long VDBP treatment. At the end of the treatment, (**I**) ROS production, (**J**) mitochondrial membrane potential, and (**K**) myotube diameters were measured as previously described; n=6 experimental replicates from three independent experiments for (I) and (J); n=3 independent experiments for (K). All treatments were in serum-free medium. Data are presented as means ± SEM. Statistical analysis: one-way

ANOVA followed by Tukey's multiple comparisons test for (A)-(F) and (I)-(K); two-tailed unpaired t-test for (H). Source data are provided as a Source Data file.

Figure 5. VDBP-induced atrophy is mediated by actin dynamics perturbation.

(**A**) VDBP accumulation in the mitochondrial fraction (Mito) was analyzed by Western blot. Relative intensity was normalized on VDAC; n=3 independent experiments. (**B**) At the end of the treatment, VDBP in the mitochondrial fraction was immunoprecipitated, and the interaction with actin was evaluated by Western blotting; representative image of n=2 independent experiments. (**C**) Recruitment of DRP1 at the mitochondria was analyzed by western blotting of the mitochondrial fraction (Mito). Relative intensity was normalized on VDAC; n=3 independent experiments. (**D**) The interaction of VDBP and DRP1 was investigated by proximity ligation assay (PLA) in C2C12 myotubes treated with VDBP in the presence or absence of 250 nM Jasplakinolide (Jas) pre-treatment. The dots inside the myotubes (identified by MyHC immunofluorescence) were quantified and normalized to control cells (-); n=3 independent experiments, combined with 2 independent experiments previously performed without Jas. Scale bar 20 μm. (**E-F**) C2C12 myotubes were treated with 50 nm VDBP in the presence or absence of 10 μM Mitochondrial division inhibitor 1 (Mdivi-1) for 24 h. At the end of treatment, (**E**) ROS production was evaluated by CellROX Deep Red reagent and quantified as fluorescence mean intensity of each myotube; n=6 experimental replicates from three independent experiments. (**F**) Myotube diameters were measured from n=3 independent experiments. (**G**) Mitochondrial morphology analysis of VDBP-treated human myotubes was performed using Mitochondria Analyzer plugin for ImageJ. Bar graph represents the mean mitochondrial area in controls and VDBP-treated cells; n=6 independent experiments. Scale bar 20 μm. (**H-I**). Human myotubes were treated with 50 nM VDBP in the presence or absence of 10 μM Mdivi-1 or after 30 min pre-treatment with 250 nM Jas. At the end of treatment, (**H**) ROS production and (**I**) myotube diameters were measured as previously described; n=3 independent experiments with Jas, combined with 3 independent experiments with Mdivi-1. All treatments were in serum-free medium. Data are presented as means ± SEM. Statistical analysis: two-tailed unpaired t-test for (A), (C), and (G); one-way ANOVA followed by Tukey's multiple comparisons test for (D)-(F) and (H) and (I). Source data are provided as a Source Data file.

Figure 6. Exogenous VDBP induction promotes muscle wasting in *Gc* KO male mice. 1.5 mg/kg VDBP was intramuscularly administered in one of the *tibialis anterior* (TA) muscles of *Gc* KO male mice every 48 h for 8 days. Contralateral muscles injected with saline (SAL) were used as controls. (**A**) Grip strength performance of the VDBP- vs. SAL-injected limbs; n=11/group; from left to right: p=0.00012, p=0.000106, p<0.00001, p<0.00001. (**B-I**) A different group of mice was euthanized after 48 h of treatment; n=4/group. (**B**) Weight of TA normalized to the tibial lengths. (**C**) Proportion of the different myofiber types (MyHC IIa, IIb, and IIx) in TA. Scale bar 800 µm. (**D**) The ratio of G- and F-actin content in TA isolated with the G-actin/F-actin In Vivo Assay Kit was evaluated by Western blotting. (**E**) Expression of *Mff,* (**F**) *Bnip3,* and (**G**) *Ppargc1a* assessed by real-time RT-PCR in TA, using *Ppif* as the housekeeping gene. (**H**) Mitochondrial content expressed as the mean intensity of TOM20 signal. (**I**) Mitochondrial morphology in TA fibers was visualized through immunofluorescence of TOM20 and mean mitochondrial area quantified using the ImageJ Mitochondria Analyzer plugin. Scale bar 20 µm. (**J**) Mitochondria respiration was measured in permeabilized TA myofibers and normalized to tissue weight; n=6/group. (**K-T**) *Gc* KO mice euthanized after 8 days of VDBP treatment. (**K**) Weight of TA normalized to the tibial lengths. (**L**) Cross-sectional area (CSA) frequency distribution of myofibers in TA. Scale bar 100 µm. (**M**) Proportion of the different

myofiber types. Scale bar 800 µm. Expression of (**N**) *Mff*, (**O**) *Bnip3*, and (**P**) *Ppargc1a* by real-time RT-PCR in TA. (**Q**) Mitochondrial content as the mean intensity of TOM20 immunofluorescence signal, and (**R**) mean mitochondrial area quantified as described above. Scale bar 20 µm. (**S**) Mitochondrial respiration in permeabilized TA myofibers normalized to tissue weight. (**T**) Free 25-hydroxy-vitamin D_3 (25VD) levels in TA were evaluated by ELISA. Data are shown as mean ± SEM; n=8/group in (K); n=6/group in (L), (N)-(P), and (S); n=5/group in (M), (Q), (R), and (T), except where outliers were excluded. Statistical analysis: multiple paired two-tailed t-tests were performed with FDR correction using the two-stage step-up method of Benjamini, Krieger and Yekutieli (Q=1%) for (A); two-tailed unpaired t-test for (B)-(T); differences in CSA distribution between groups were assessed using a chi-square goodness-of-fit test, with SAL frequencies as the expected distribution. Source data are provided as a Source Data file.

Figure 7. Lack of VDBP attenuates muscle wasting in the LLC cancer cachexia model in male mice. (**A**) VDBP expression in the liver measured by real-time RT-PCR in saline-injected (SAL; n=8) and LLC-bearing (LLC; n = 9) wild-type (WT) mice 23 days after cell injection, and in LLC tumors (n=7). (**B**) Circulating VDBP was quantified by ELISA in WT mice before LLC cell injection and at the end of the experiment (n=11). (**C**) Total and free 25VD was measured in the blood and gastrocnemius muscles of WT and *Gc* KO saline-injected controls (SAL WT and *Gc* KO: n=5 for total and free VD in blood, 3 for total VD and 4 for free VD in muscle) and LLC-bearing mice (n=5 for each group) using LC-MS and a specific ELISA, respectively. (**D**) Grip strength performance was recorded immediately before LLC cell injection and monitored until the day of sacrifice; n=7 (WT) and 6 (*Gc* KO); *p=0.0134, ***p=0.00029. (**E**) Endurance measured through a treadmill run. The bars represent the total distance covered till exhaustion;

n=7 (WT) and 8 (*Gc* KO). (**F**) Tumor-free body weight at the endpoint; n=7 (WT) and 8 (*Gc* KO) for each group. (**G**) Weight of tibialis anterior (TA), gastrocnemius (GAS), and quadriceps (QUAD) at the endpoint; n=5 (SAL WT and *Gc* KO), 7 (LLC WT), and 8 (LLC *Gc* KO). (**H**) Representative images and CSA frequency distribution of myofibers in GAS of tumor-bearing mice; n=5 for each group. Scale bar 100 µm. (**I-K**) Relative expression of (**I**) *Fbxo32*, (**J**) *Bnip3*, and (**K**) *Mff* in GAS of control or tumor-bearing mice by real-time RT-PCR using *Ppif* as the housekeeping gene; n=4 for SAL WT, 5 for the other groups, except where outliers were excluded. (**L**) Representative images of mitochondria visualized by TOM20 immunofluorescence and quantification of their area with ImageJ Mitochondria Analyzer plugin; n=3 for the SAL groups and 5 for the LLC groups. Scale bar 20 µm. (**M**) Mitochondrial respiration measured in permeabilized GAS myofibers and normalized to tissue weight; SAL n=7 (WT) and 5 (*Gc* KO), LLC n=5 (WT), and 4 (*Gc* KO). (**N**) Acetylcholine receptor (AChR) cluster area and innervation were evaluated through α-bungarotoxin staining and immunofluorescence targeting the neurofilament (NF-1) in EDL muscles. NMJ quantification was obtained by analyzing 31 NMJs in WT SAL, 16 in *Gc* KO SAL, 31 in WT LLC, and 31 in *Gc* KO LLC. Scale bar 20 µm. Data are presented as means ± SEM. Statistical analysis: two-tailed unpaired t-test for (A) and (E); two-tailed paired t-test for (B); one-way ANOVA followed by Tukey's multiple comparisons test for (C), (F), (G), and (I)-(N); multiple unpaired two-tailed t-tests were performed with FDR correction using the two-stage step-up method of Benjamini, Krieger and Yekutieli (Q=1%) for (D); differences in CSA distribution between groups were assessed using a chi-square goodness-of-fit test, with WT frequencies as the expected distribution. Source data are provided as a Source Data file.

Figure 8. RNA-seq analysis of cachectic WT and *Gc* KO male mice. RNA-seq analysis of gastrocnemii from tumor-bearing mice (LCC) compared with corresponding controls (SAL) in WT and *Gc* KO mice was performed to evaluate the impact of VDBP on cancer-associated muscle wasting; SAL n = 3 for each group and LLC n = 7 (WT) and 6 (*Gc* KO). (**A**) Heatmaps of differentially expressed genes (DEGs; $|\log_2$ fold change$| > 1.5$ and FDR < 0.1) characterizing cachexia in the two genotypes. (**B**) Venn diagrams showing the comparison between tumor-induced upregulated and downregulated DEGs in WT and *Gc* KO muscles. (**C**) Enriched gene sets in WT LLC vs. *Gc* KO LLC resulting from gene set enrichment analysis (GSEA). A positive Normalized Enrichment Score (NES) value indicates enrichment in the WT LLC mice (orange bars), whereas a negative NES indicates enrichment in the *Gc* KO LLC ones (blue bars). Source data are provided in Supplementary Data 3 and available in the NCBI GEO.

Editorial Summary

The study demonstrates that vitamin D binding protein causes skeletal muscle atrophy and plays a role in cancer-related muscle wasting, regardless of vitamin D levels in preclinical models.

Peer review information: *Nature Communications* thanks the anonymous reviewer(s) for their contribution to the peer review of this work. A peer review file is available.

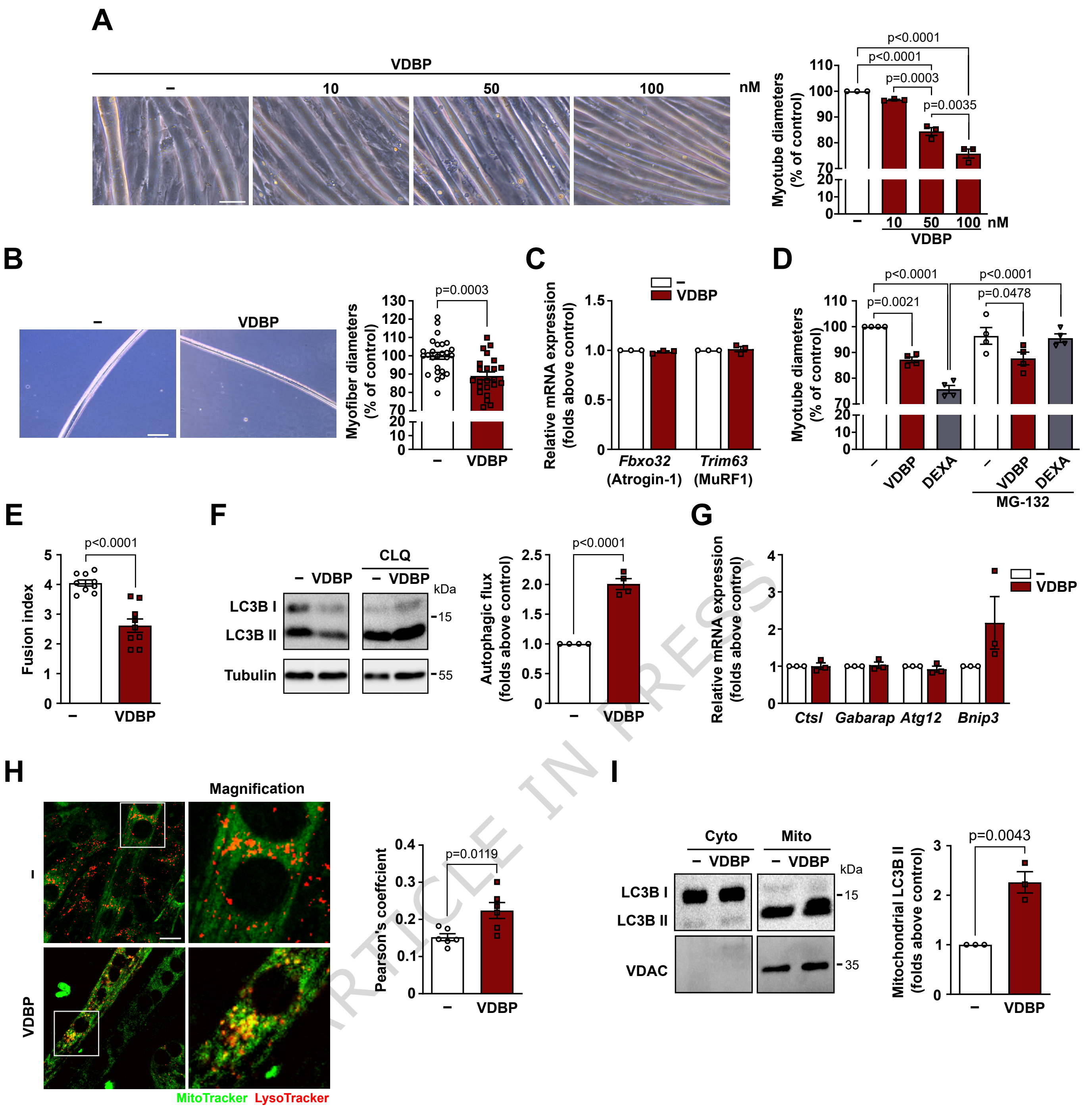
A
VDBP
–
10
50
100
nM
Myotube diameters (% of control)
p<0.0001
p<0.0001
p=0.0003
p=0.0035
110
100
90
80
70
20
10
0
–
10
50
100
nM
VDBP
B
–
VDBP
Myofiber diameters (% of control)
p=0.0003
130
120
110
100
90
80
70
20
10
0
–
VDBP
C
–
VDBP
Relative mRNA expression (folds above control)
1.5
1.0
0.5
0
Fbxo32 (Atrogin-1)
Trim63 (MuRF1)
D
Myotube diameters (% of control)
p<0.0001
p=0.0021
p<0.0001
p=0.0478
110
100
90
80
70
20
10
0
–
VDBP
DEXA
–
VDBP
DEXA
MG-132
E
Fusion index
p<0.0001
5
4
3
2
1
0
–
VDBP
F
CLQ
– VDBP
– VDBP
kDa
LC3B I
LC3B II
-15
Tubulin
-55
Autophagic flux (folds above control)
p<0.0001
2.5
2.0
1.5
1.0
0.5
0
–
VDBP
G
Relative mRNA expression (folds above control)
4
3
2
1
0
–
VDBP
Ctsl
Gabarap
Atg12
Bnip3
H
Magnification
–
VDBP
MitoTracker
LysoTracker
Pearson's coefficient
p=0.0119
0.4
0.3
0.2
0.1
0
–
VDBP
I
Cyto
Mito
– VDBP
– VDBP
kDa
LC3B I
LC3B II
-15
VDAC
-35
Mitochondrial LC3B II (folds above control)
p=0.0043
3
2
1
0
–
VDBP

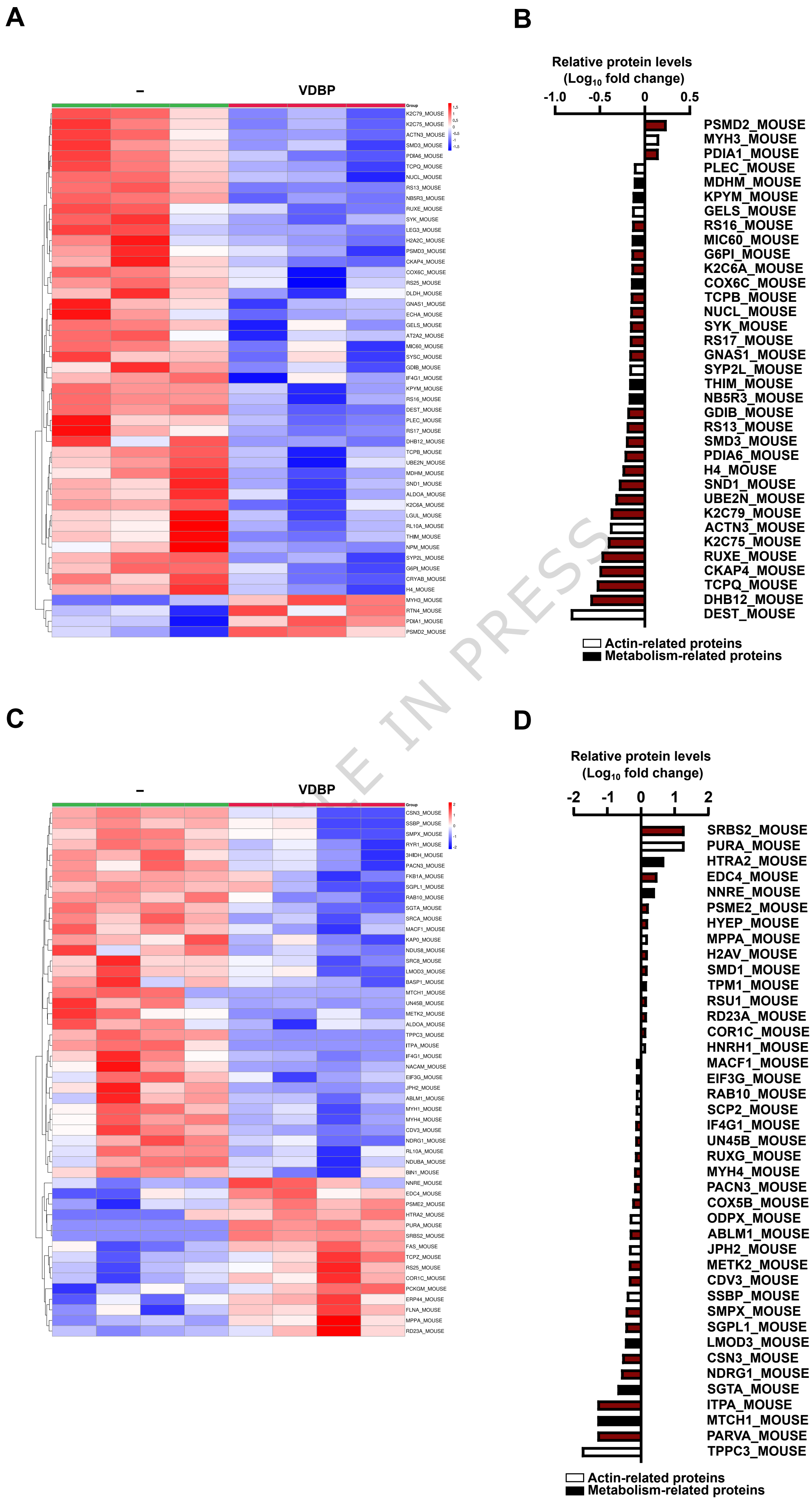
A
–
VDBP
Group
1.5
1
0.5
0
-0.5
-1
-1.5
K2C79_MOUSE
K2C75_MOUSE
ACTN3_MOUSE
SMD3_MOUSE
PDIA6_MOUSE
TCPQ_MOUSE
NUCL_MOUSE
RS13_MOUSE
NB5R3_MOUSE
RUXE_MOUSE
SYK_MOUSE
LEG3_MOUSE
H2A2C_MOUSE
PSMD3_MOUSE
CKAP4_MOUSE
COX6C_MOUSE
RS25_MOUSE
DLDH_MOUSE
GNAS1_MOUSE
ECHA_MOUSE
GELS_MOUSE
AT2A2_MOUSE
MIC60_MOUSE
SYSC_MOUSE
GDIB_MOUSE
IF4G1_MOUSE
KPYM_MOUSE
RS16_MOUSE
DEST_MOUSE
PLEC_MOUSE
RS17_MOUSE
DHB12_MOUSE
TCPB_MOUSE
UBE2N_MOUSE
MDHM_MOUSE
SND1_MOUSE
ALDOA_MOUSE
K2C6A_MOUSE
LGUL_MOUSE
RL10A_MOUSE
THIM_MOUSE
NPM_MOUSE
SYP2L_MOUSE
G6PI_MOUSE
CRYAB_MOUSE
H4_MOUSE
MYH3_MOUSE
RTN4_MOUSE
PDIA1_MOUSE
PSMD2_MOUSE
B
Relative protein levels
(Log_{10} fold change)
-1.0
-0.5
0
0.5
PSMD2_MOUSE
MYH3_MOUSE
PDIA1_MOUSE
PLEC_MOUSE
MDHM_MOUSE
KPYM_MOUSE
GELS_MOUSE
RS16_MOUSE
MIC60_MOUSE
G6PI_MOUSE
K2C6A_MOUSE
COX6C_MOUSE
TCPB_MOUSE
NUCL_MOUSE
SYK_MOUSE
RS17_MOUSE
GNAS1_MOUSE
SYP2L_MOUSE
THIM_MOUSE
NB5R3_MOUSE
GDIB_MOUSE
RS13_MOUSE
SMD3_MOUSE
PDIA6_MOUSE
H4_MOUSE
SND1_MOUSE
UBE2N_MOUSE
K2C79_MOUSE
ACTN3_MOUSE
K2C75_MOUSE
RUXE_MOUSE
CKAP4_MOUSE
TCPQ_MOUSE
DHB12_MOUSE
DEST_MOUSE
☐ Actin-related proteins
■ Metabolism-related proteins
C
–
VDBP
Group
2
1
0
-1
-2
CSN3_MOUSE
SSBP_MOUSE
SMPX_MOUSE
RYR1_MOUSE
3HIDH_MOUSE
PACN3_MOUSE
FKB1A_MOUSE
SGPL1_MOUSE
RAB10_MOUSE
SGTA_MOUSE
SRCA_MOUSE
MACF1_MOUSE
KAP0_MOUSE
NDUS8_MOUSE
SRC8_MOUSE
LMOD3_MOUSE
BASP1_MOUSE
MTCH1_MOUSE
UN45B_MOUSE
METK2_MOUSE
ALDOA_MOUSE
TPPC3_MOUSE
ITPA_MOUSE
IF4G1_MOUSE
NACAM_MOUSE
EIF3G_MOUSE
JPH2_MOUSE
ABLM1_MOUSE
MYH1_MOUSE
MYH4_MOUSE
CDV3_MOUSE
NDRG1_MOUSE
RL10A_MOUSE
NDUBA_MOUSE
BIN1_MOUSE
NNRE_MOUSE
EDC4_MOUSE
PSME2_MOUSE
HTRA2_MOUSE
PURA_MOUSE
SRBS2_MOUSE
FAS_MOUSE
TCPZ_MOUSE
RS25_MOUSE
COR1C_MOUSE
PCKGM_MOUSE
ERP44_MOUSE
FLNA_MOUSE
MPPA_MOUSE
RD23A_MOUSE
D
Relative protein levels
(Log_{10} fold change)
-2
-1
0
1
2
SRBS2_MOUSE
PURA_MOUSE
HTRA2_MOUSE
EDC4_MOUSE
NNRE_MOUSE
PSME2_MOUSE
HYEP_MOUSE
MPPA_MOUSE
H2AV_MOUSE
SMD1_MOUSE
TPM1_MOUSE
RSU1_MOUSE
RD23A_MOUSE
COR1C_MOUSE
HNRH1_MOUSE
MACF1_MOUSE
EIF3G_MOUSE
RAB10_MOUSE
SCP2_MOUSE
IF4G1_MOUSE
UN45B_MOUSE
RUXG_MOUSE
MYH4_MOUSE
PACN3_MOUSE
COX5B_MOUSE
ODPX_MOUSE
ABLM1_MOUSE
JPH2_MOUSE
METK2_MOUSE
CDV3_MOUSE
SSBP_MOUSE
SMPX_MOUSE
SGPL1_MOUSE
LMOD3_MOUSE
CSN3_MOUSE
NDRG1_MOUSE
SGTA_MOUSE
ITPA_MOUSE
MTCH1_MOUSE
PARVA_MOUSE
TPPC3_MOUSE
☐ Actin-related proteins
■ Metabolism-related proteins

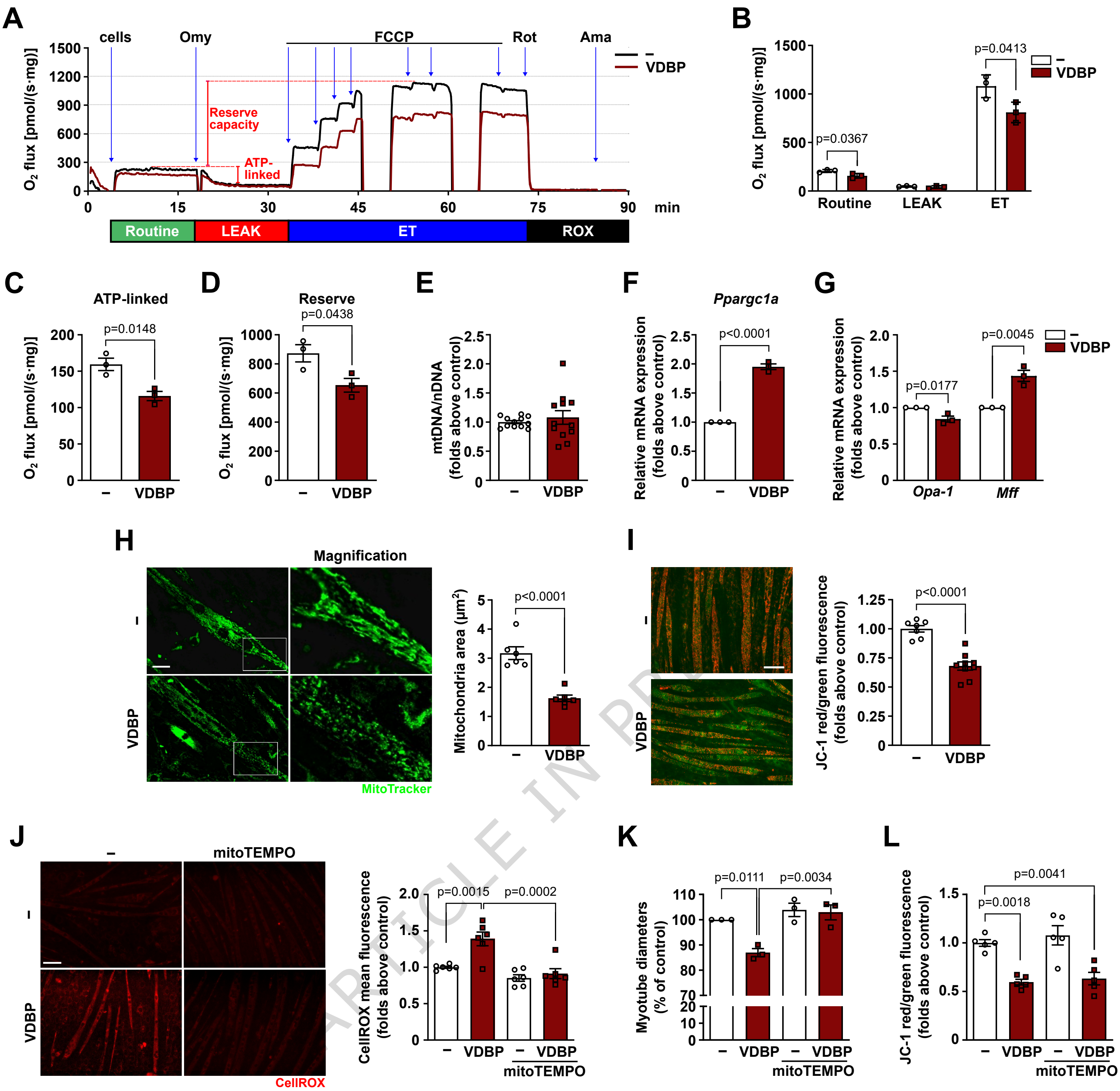
A
cells
Omy
FCCP
Rot
Ama
–
VDBP
O2 flux [pmol/(s·mg)]
1500
1200
900
600
300
0
Reserve capacity
ATP-linked
0
15
30
45
60
75
90
min
Routine
LEAK
ET
ROX
B
1500
1000
500
0
p=0.0367
p=0.0413
Routine
LEAK
ET
C
ATP-linked
p=0.0148
200
150
100
50
0
D
Reserve
p=0.0438
1000
800
600
400
200
0
E
mtDNA/nDNA (folds above control)
2.5
2.0
1.5
1.0
0.5
0
F
Ppargc1a
Relative mRNA expression (folds above control)
p<0.0001
G
p=0.0177
p=0.0045
Opa-1
Mff
H
Magnification
Mitochondria area (µm²)
p<0.0001
5
4
3
2
1
0
MitoTracker
I
JC-1 red/green fluorescence (folds above control)
p<0.0001
1.25
1.00
0.75
0.50
0.25
0
J
mitoTEMPO
CellROX mean fluorescence (folds above control)
p=0.0015
p=0.0002
CellROX
K
Myotube diameters (% of control)
p=0.0111
p=0.0034
110
100
90
80
70
20
10
0
L
JC-1 red/green fluorescence (folds above control)
p=0.0018
p=0.0041
1.5
1.0
0.5
0

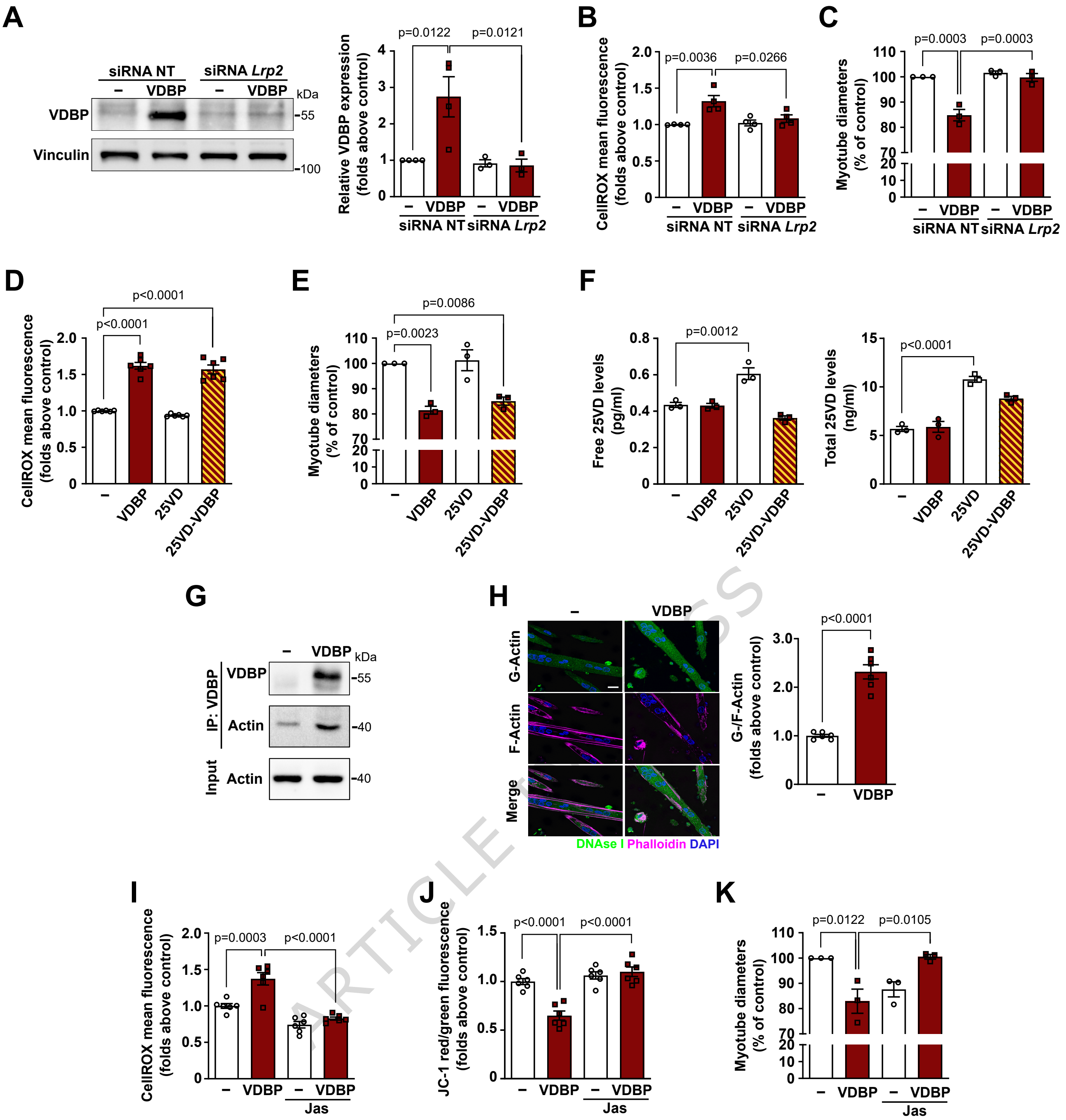
A
siRNA NT
siRNA Lrp2
–
VDBP
–
VDBP
kDa
VDBP
-55
Vinculin
-100
Relative VDBP expression (folds above control)
p=0.0122
p=0.0121
4
3
2
1
0
–
VDBP
–
VDBP
siRNA NT
siRNA Lrp2
B
CellROX mean fluorescence (folds above control)
2.0
1.5
1.0
0.5
0
p=0.0036
p=0.0266
–
VDBP
–
VDBP
siRNA NT
siRNA Lrp2
C
Myotube diameters (% of control)
p=0.0003
p=0.0003
110
100
90
80
70
20
10
0
–
VDBP
–
VDBP
siRNA NT
siRNA Lrp2
D
CellROX mean fluorescence (folds above control)
p<0.0001
p<0.0001
2.0
1.5
1.0
0.5
0
–
VDBP
25VD
25VD-VDBP
E
Myotube diameters (% of control)
p=0.0086
p=0.0023
110
100
90
80
70
20
10
0
–
VDBP
25VD
25VD-VDBP
F
Free 25VD levels (pg/ml)
p=0.0012
0.8
0.6
0.4
0.2
0
–
VDBP
25VD
25VD-VDBP
Total 25VD levels (ng/ml)
p<0.0001
15
10
5
0
–
VDBP
25VD
25VD-VDBP
G
–
VDBP
kDa
IP: VDBP
VDBP
-55
Actin
-40
Input
Actin
-40
H
–
VDBP
G-Actin
F-Actin
Merge
DNAse I
Phalloidin
DAPI
G-/F-Actin (folds above control)
p<0.0001
3.0
2.0
1.0
0
–
VDBP
I
CellROX mean fluorescence (folds above control)
p=0.0003
p<0.0001
2.0
1.5
1.0
0.5
0
–
VDBP
–
VDBP
Jas
J
JC-1 red/green fluorescence (folds above control)
p<0.0001
p<0.0001
1.5
1.0
0.5
0
–
VDBP
–
VDBP
Jas
K
Myotube diameters (% of control)
p=0.0122
p=0.0105
110
100
90
80
70
20
10
0
–
VDBP
–
VDBP
Jas

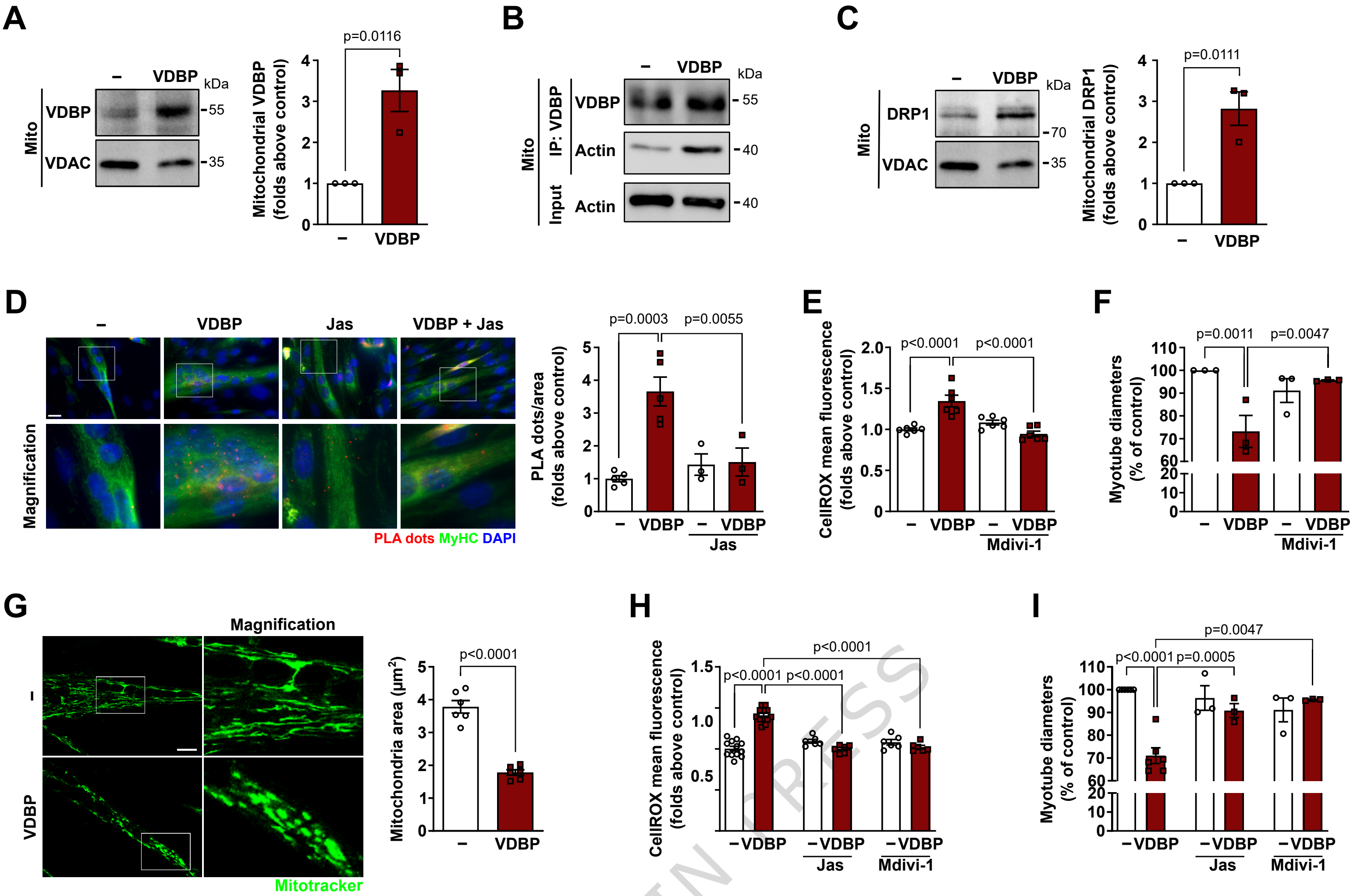
A
–
VDBP
kDa
Mito
VDBP
VDAC
55
35
Mitochondrial VDBP (folds above control)
p=0.0116
0
1
2
3
4
–
VDBP
B
–
VDBP
kDa
Mito
IP: VDBP
Input
VDBP
Actin
Actin
55
40
40
C
–
VDBP
kDa
Mito
DRP1
VDAC
70
35
Mitochondrial DRP1 (folds above control)
p=0.0111
0
1
2
3
4
–
VDBP
D
–
VDBP
Jas
VDBP + Jas
Magnification
PLA dots MyHC DAPI
PLA dots/area (folds above control)
p=0.0003
p=0.0055
0
1
2
3
4
5
–
VDBP
–
VDBP
Jas
E
CellROX mean fluorescence (folds above control)
p<0.0001
p<0.0001
0
0.5
1.0
1.5
2.0
–
VDBP
–
VDBP
Mdivi-1
F
Myotube diameters (% of control)
p=0.0011
p=0.0047
0
10
20
60
70
80
90
100
110
–
VDBP
–
VDBP
Mdivi-1
G
Magnification
–
VDBP
Mitotracker
Mitochondria area (μm²)
p<0.0001
0
1
2
3
4
5
–
VDBP
H
CellROX mean fluorescence (folds above control)
p<0.0001
p<0.0001
p<0.0001
0.5
1.0
1.5
–VDBP
–VDBP
Jas
–VDBP
Mdivi-1
I
Myotube diameters (% of control)
p=0.0047
p<0.0001
p=0.0005
0
10
20
60
70
80
90
100
110
–VDBP
–VDBP
Jas
–VDBP
Mdivi-1

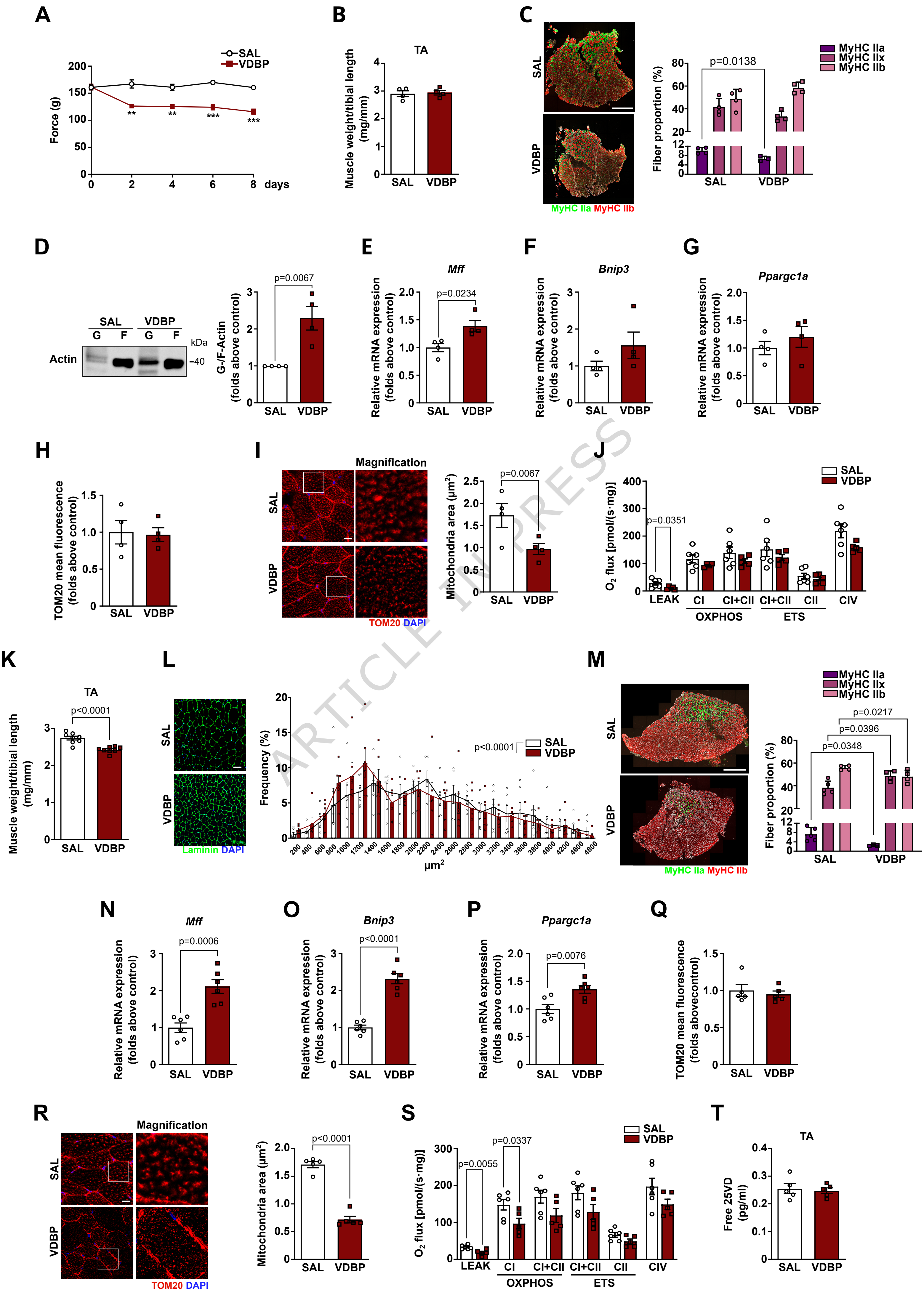
A
SAL
VDBP
Force (g)
200
150
100
50
0
**
**
***
***
0 2 4 6 8 days
B
TA
Muscle weight/tibial length (mg/mm)
4 3 2 1 0
SAL VDBP
C
SAL
VDBP
MyHC IIa MyHC IIb
p=0.0138
Fiber proportion (%)
80 60 40 20 12 8 4 0
MyHC IIa
MyHC IIx
MyHC IIb
SAL VDBP
D
SAL VDBP
G F G F
kDa
Actin
-40
p=0.0067
G-/F-Actin (folds above control)
3 2 1 0
SAL VDBP
E
Mff
p=0.0234
Relative mRNA expression (folds above control)
2.0 1.5 1.0 0.5 0
SAL VDBP
F
Bnip3
Relative mRNA expression (folds above control)
3 2 1 0
SAL VDBP
G
Ppargc1a
Relative mRNA expression (folds above control)
2.0 1.5 1.0 0.5 0
SAL VDBP
H
TOM20 mean fluorescence (folds above control)
1.5 1.0 0.5 0
SAL VDBP
I
Magnification
SAL
VDBP
TOM20 DAPI
p=0.0067
Mitochondria area (µm²)
2.5 2.0 1.5 1.0 0.5 0
SAL VDBP
J
SAL
VDBP
O₂ flux [pmol/(s·mg)]
400 300 200 100 0
p=0.0351
LEAK CI CI+CII CI+CII CII CIV
OXPHOS ETS
K
TA
p<0.0001
Muscle weight/tibial length (mg/mm)
3 2 1 0
SAL VDBP
L
SAL
VDBP
Laminin DAPI
Frequency (%)
20 15 10 5 0
p<0.0001
SAL
VDBP
200 400 600 800 1000 1200 1400 1600 1800 2000 2200 2400 2600 2800 3000 3200 3400 3600 3800 4000 4200 4600 4800
µm²
M
SAL
VDBP
MyHC IIa MyHC IIb
MyHC IIa
MyHC IIx
MyHC IIb
p=0.0217
p=0.0396
p=0.0348
Fiber proportion (%)
80 60 40 20 12 8 4 0
SAL VDBP
N
Mff
p=0.0006
Relative mRNA expression (folds above control)
3 2 1 0
SAL VDBP
O
Bnip3
p<0.0001
Relative mRNA expression (folds above control)
3 2 1 0
SAL VDBP
P
Ppargc1a
p=0.0076
Relative mRNA expression (folds above control)
2.0 1.5 1.0 0.5 0
SAL VDBP
Q
TOM20 mean fluorescence (folds abovecontrol)
1.5 1.0 0.5 0
SAL VDBP
R
Magnification
SAL
VDBP
TOM20 DAPI
p<0.0001
Mitochondria area (µm²)
2.0 1.5 1.0 0.5 0
SAL VDBP
S
SAL
VDBP
O₂ flux [pmol/(s·mg)]
300 200 100 0
p=0.0055
p=0.0337
LEAK CI CI+CII CI+CII CII CIV
OXPHOS ETS
T
TA
Free 25VD (pg/ml)
0.4 0.3 0.2 0.1 0
SAL VDBP

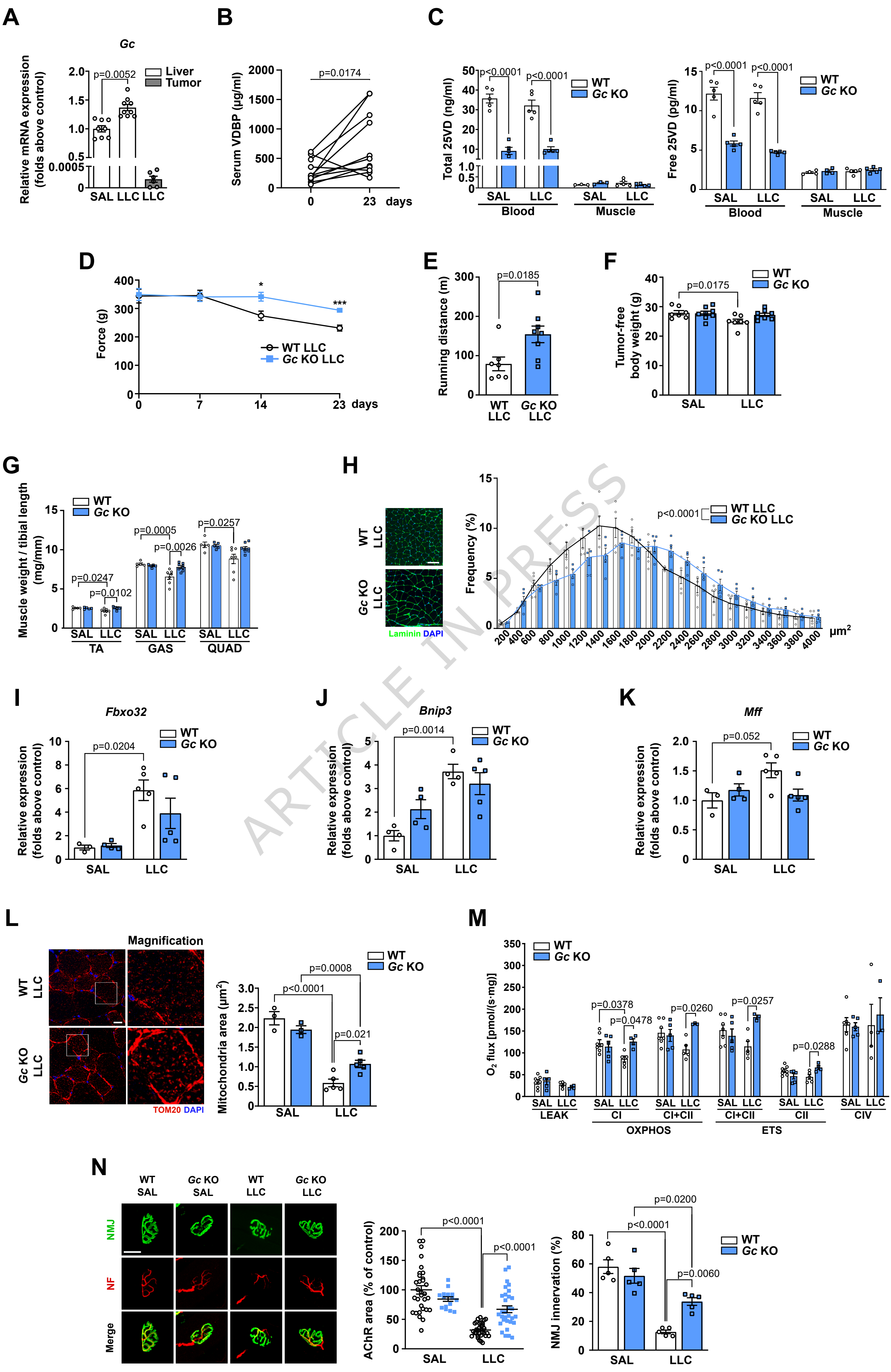
A
Gc
Relative mRNA expression (folds above control)
Liver
Tumor
p=0.0052
2.0
1.5
1.0
0.5
0.0005
0
SAL LLC LLC
B
Serum VDBP (µg/ml)
p=0.0174
2000
1500
1000
500
0
0
23 days
C
Total 25VD (ng/ml)
p<0.0001
p<0.0001
WT
Gc KO
50
40
30
20
10
1.0
0.5
0
SAL LLC
Blood
SAL LLC
Muscle
Free 25VD (pg/ml)
p<0.0001
p<0.0001
15
10
5
0
D
Force (g)
400
300
200
100
0
0 7 14 23 days
*
***
WT LLC
Gc KO LLC
E
Running distance (m)
p=0.0185
300
200
100
0
WT LLC
Gc KO LLC
F
Tumor-free body weight (g)
p=0.0175
40
30
20
10
0
SAL
LLC
G
Muscle weight / tibial length (mg/mm)
15
10
5
0
p=0.0247
p=0.0102
p=0.0005
p=0.0026
p=0.0257
SAL LLC
TA
GAS
QUAD
H
WT LLC
Gc KO LLC
Laminin DAPI
Frequency (%)
p<0.0001
WT LLC
Gc KO LLC
200 400 600 800 1000 1200 1400 1600 1800 2000 2200 2400 2600 2800 3000 3200 3400 3600 3800 4000
µm²
I
Fbxo32
Relative expression (folds above control)
p=0.0204
10
8
6
4
2
0
SAL
LLC
J
Bnip3
p=0.0014
5
4
3
2
1
0
K
Mff
p=0.052
2.0
1.5
1.0
0.5
0
L
Magnification
WT LLC
Gc KO LLC
TOM20 DAPI
Mitochondria area (µm²)
p=0.0008
p<0.0001
p=0.021
3.0
2.5
2.0
1.5
1.0
0.5
0
M
O2 flux [pmol/(s·mg)]
350
300
250
200
150
100
50
0
p=0.0378
p=0.0478
p=0.0260
p=0.0257
p=0.0288
LEAK
CI
CI+CII
CI+CII
CII
CIV
OXPHOS
ETS
N
WT SAL
Gc KO SAL
WT LLC
Gc KO LLC
NMJ
NF
Merge
AChR area (% of control)
p<0.0001
p<0.0001
200
150
100
50
0
NMJ innervation (%)
p=0.0200
p<0.0001
p=0.0060
80
60
40
20
0
WT
Gc KO

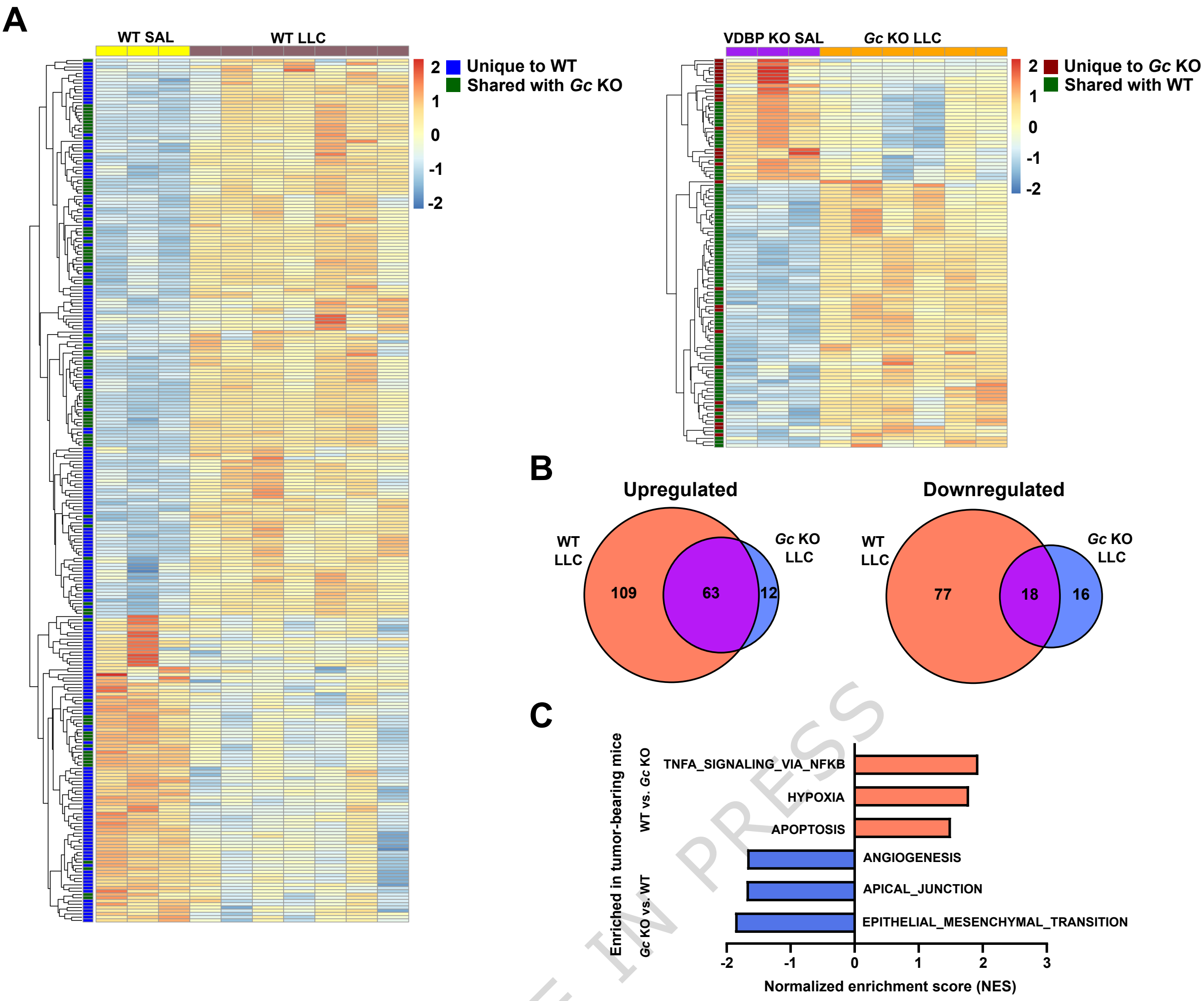
A
WT SAL
WT LLC
2
1
0
-1
-2
Unique to WT
Shared with *Gc* KO
VDBP KO SAL
Gc KO LLC
Unique to *Gc* KO
Shared with WT
B
Upregulated
WT LLC
Gc KO LLC
109
63
12
Downregulated
WT LLC
Gc KO LLC
77
18
16
C
Enriched in tumor-bearing mice
WT vs. *Gc* KO
Gc KO vs. WT
TNFA_SIGNALING_VIA_NFKB
HYPOXIA
APOPTOSIS
ANGIOGENESIS
APICAL_JUNCTION
EPITHELIAL_MESENCHYMAL_TRANSITION
-2
-1
0
1
2
3
Normalized enrichment score (NES)